# Clarin-2 gene supplementation durably preserves hearing in a model of progressive hearing loss

Clara Mendia, Thibault Peineau, Mina Zamani, Chloé Felgerolle, Nawal Yahiaoui, Nele Christophersen, Samantha Papal, Audrey Maudoux, Reza Maroofian, Pranav Patni, et al.

Molecular Therapy
Original Article

# Clarin-2 gene supplementation durably preserves hearing in a model of progressive hearing loss

Clara Mendia,[1,2,9] Thibault Peineau,[3,9] Mina Zamani,[4] Chloé Felgerolle,[1] Nawal Yahiaoui,[1] Nele Christophersen,[5,6] Samantha Papal,[1] Audrey Maudoux,[1] Reza Maroofian,[7] Pranav Patni,[1] Sylvie Nouaille,[1] Michael R. Bowl,[8] Sedigheh Delmaghani,[1] Hamid Galehdari,[4] Barbara Vona,[5,6] Didier Dulon,[3] Sandrine Vitry,[1,10] and Aziz El-Amraoui[1,10]

[1]Institut Pasteur, Université Paris Cité, INSERM AO06, Institut de l'Audition, Unit Progressive Sensory Disorders, Pathophysiology and Therapy, 63 rue de Charenton, 75012 Paris, France; [2]Sorbonne Université, Collège Doctoral, 75005 Paris, France; [3]Institut de l'Audition and Université de Bordeaux, Laboratoire de Neurophysiologie de la Synapse Auditive, Bordeaux Neurocampus, 33076 Bordeaux, France; [4]Department of Biology, Faculty of Science, Shahid Chamran University of Ahvaz, Ahvaz 6135783151, Iran; [5]Institute for Auditory Neuroscience and InnerEarLab, University Medical Center Göttingen, 37075 Göttingen, Germany; [6]Institute of Human Genetics, University Medical Center Göttingen, 37075 Göttingen, Germany; [7]Department of Neuromuscular Diseases, UCL Queen Square Institute of Neurology, University College London, WC1E 6BT London, UK; [8]UCL Ear Institute, University College London, 332 Gray's Inn Road, WC1X 8EE London, UK

**Hearing loss is a major health concern affecting millions of people worldwide with currently limited treatment options. In clarin-2-deficient *Clrn2*$^{-/-}$ mice, used here as a model of progressive hearing loss, we report synaptic auditory abnormalities in addition to the previously demonstrated defects of hair bundle structure and mechanoelectrical transduction. We sought an in-depth evaluation of viral-mediated gene delivery as a therapy for these hearing-impaired mice. Supplementation with either the murine *Clrn2* or human *CLRN2* genes preserved normal hearing in treated *Clrn2*$^{-/-}$ mice. Conversely, mutated forms of *CLRN2*, identified in patients with post-lingual moderate to severe hearing loss, failed to prevent hearing loss. The ectopic expression of clarin-2 successfully prevented the loss of stereocilia, maintained normal mechanoelectrical transduction, preserved inner hair cell synaptic function, and ensured near-normal hearing thresholds over time. Maximal hearing preservation was observed when *Clrn2* was delivered prior to the loss of transducing stereocilia. Our findings demonstrate that gene therapy is effective for the treatment of post-lingual hearing impairment and age-related deafness associated with *CLRN2* patient mutations.**

## INTRODUCTION

Hearing impairment is the most common sensory disorder worldwide, affecting almost 500 million people globally. Inherited forms affect approximately 1.3 in 1,000 newborns, and the incidence of hearing loss increases with age, with 70% of people over the age of 70 years affected.[1–3] Hearing loss can have severe consequences, including social isolation, communication difficulties, cognitive decline, and depression.[4] It also has significant economic implications, with a global annual cost of unaddressed hearing loss estimated at over US$981 billion.[2] Despite the significant societal and economic consequences of hearing loss, effective biological treatments for cochlear dysfunction are still lacking.[1,3,5] Cochlear implants—electronic devices that stimulate the auditory nerve conveying the sensation of sound to the central nervous system—are currently the primary treatment for severe hearing loss.[6] They can reduce the burden of hearing loss but do not restore normal auditory function and the ability to discriminate speech correctly or appreciate music. Moreover, they are subject to several limitations, including high costs, risks of surgical complications, and limited benefit in some patients, particularly those with residual hearing.

The lack of effective biological treatments for hearing loss has spurred a growing interest in gene therapy as a potential therapeutic approach.[1,3,7] Several promising studies have investigated the potential application of adeno-associated virus (AAV)-mediated gene therapy in the inner ear.[8–13] However, these studies often reported only a partial recovery of Hring, mostly in the low-frequency range.[8–11,14] Indeed, several core challenges still hamper the achievement of full auditory function recovery. These include efficacy and long-term stability of the therapeutic agent, the degree of recovery over the full frequency range, and identification of the optimal therapeutic window for treatment.

Received 20 October 2023; accepted 12 January 2024;
https://doi.org/10.1016/j.ymthe.2024.01.021.

[9]These authors contributed equally

[10]Senior author

**Correspondence:** Dr Sandrine Vitry, Unit Progressive Sensory Disorders, Pathophysiology and Therapy, Institut Pasteur, Institut de l'Audition, Paris, France.
**E-mail:** sandrine.vitry@pasteur.fr
**Correspondence:** Dr Aziz El Amraoui, Unit Progressive Sensory Disorders, Pathophysiology and Therapy, Institut Pasteur, Institut de l'Audition, Paris, France.
**E-mail:** aziz.el-amraoui@pasteur.fr

 

We addressed these challenges in a model of postnatal severe to profound hearing loss due to defects of a recently identified deafness gene, *CLRN2*, encoding a tetraspanin-like protein, clarin-2.[15,16] Clarin-2 belongs to the clarin family, which has three members, including CLRN1, whose defect is causal for Usher syndrome type III (USH3) and clinically manifests as post-lingual progressive deafness combined with balance and vision deficits of variable onset, progression, and severity.[10] The two clarin genes *CLRN1* and *CLRN2* encode proteins playing crucial roles in auditory hair cell function.[10,15–17] In humans, mice, and zebrafish, loss of clarin-2 function causes hearing deficits, without balance or vision defects,[15,16] reflecting the evolutionary conservation of this protein function in the cochlea. Recent genome-wide studies in large cohorts of patients have also identified *CLRN2* as a potential contributor to hearing problems in adults.[15,18] These findings support a key role for clarin-2 in the maintenance of hearing over time and provide additional support for *CLRN2* as an important target in the development of effective biological treatments for hearing loss.

In this study, we implemented the previously established defects of auditory hair bundle structure and function in *Clrn2*$^{-/-}$ mice. Our deep phenotyping revealed auditory synapse abnormalities and provided a complete and robust baseline to assess therapeutics. We then used a multiscale approach to evaluate and validate potential inner ear treatments for clarin-2-mediated progressive hearing loss. Gene supplementation in *Clrn2*$^{-/-}$ mice, using either the mouse *Clrn2* or human *CLRN2* wild-type genes, preserved near-normal hearing, whereas the transfer of pathogenic *CLRN2* variants did not. The ectopic expression of clarin-2 successfully prevented the loss of stereocilia involved in mechanoelectrical transduction (MET), maintained normal MET activity in auditory hair cells, and preserved inner hair cell (IHC) synaptic function, ensuring a durable preservation of hearing. These findings provide valuable insight into the genetic mechanisms underlying hearing loss due to pathogenic variants of *CLRN2* and further highlight the feasibility of virus-mediated gene therapy to preserve hearing function in patients with *CLRN2* mutations.

## RESULTS

### Deafness in *Clrn2*$^{-/-}$ mice is associated with hair bundle defects and synaptic dysfunction

Human hearing relies on two types of cochlear hair cells: IHCs, which are the genuine auditory sensory cells that transmit their encoded sensory signal, through their ribbon synapses, to afferent auditory nerve fibers connecting to the central nervous system (CNS); and outer hair cells (OHCs), which function as fine-tuned mechanical amplifiers of sound stimuli. We thoroughly characterized *Clrn2*$^{clarinet/clarinet}$ mice, which bear an exon 1 stop mutation and are hereafter referred to as *Clrn2*$^{-/-}$ mice (Figure 1A), to establish a complete and robust baseline for potential hearing rescue. We recently showed that *Clrn2*$^{-/-}$ mice develop rapidly progressing severe to profound hearing loss.[15] Morphological and functional analyses of the auditory hair cells of *Clrn2*$^{-/-}$ mice revealed reduced MET activity and a progressive loss of the shortest row of transducing stereocilia in hair bundles of both IHCs and OHCs (Figures 1B and S1A–S1C).[15,16] Audiometric tests showed that P30 *Clrn2*$^{-/-}$ mice had no detectable auditory brainstem response (ABR) at any frequency tested (Figure 1C). No apparent defect in the number or organization of ribbon synapses was found in *Clrn2*$^{-/-}$ IHCs.[15] However, given the known essential role of clarin-1 in maintaining efficient $Ca^{2+}$-dependent IHC synaptic vesicle exocytosis,[10] we investigated whether the lack of clarin-2 also affected IHC synaptic features. We used whole-cell time-resolved membrane capacitance measurements to explore possible IHC presynaptic exocytosis defects in P30 *Clrn2*$^{-/-}$ mice (Figures 1D–1F). We found that the resting membrane capacitance (Cm) at a holding membrane potential of −70 mV was significantly lower in *Clrn2*$^{-/-}$ IHCs compared to control IHCs (Figure 1D; $p = 0.0002$, t test), reflecting a decrease in cell membrane surface (cell size) probably due to abnormal membrane trafficking. We then recorded $Ca^{2+}$ currents ($I_{Ca}{}^{2+}$) and exocytosis ($DC_m$) during 25-ms voltage-step stimulations (Figure 1E) to probe membrane fusion of the readily releasable pool (RRP) of synaptic vesicles upon voltage-dependent activation of $Ca^{2+}$ channels. Although *Clrn2*$^{-/-}$ IHCs had $Ca^{2+}$ current densities similar to that of wild-type IHCs, their voltage-activation curve displayed a large negative shift (see $V_{1/2}$ values in Figure 1F, top left; $p < 0.0001$, t test). In parallel, amplitude of synaptic vesicle exocytosis was significantly reduced in *Clrn2*$^{-/-}$ IHCs (Figure 1F, bottom left; $p = 0.025$, Mann-Whitney test). Exocytosis kinetics (Figure 1F, top right) indicated a lower rate of RRP exocytosis in *Clrn2*$^{-/-}$ IHCs for brief stimulations (5–40 ms) ($p < 0.05$, Kruskal-Wallis test), in contrast with the secondary slow release of synaptic vesicles (slow-releasing pool [SRP]) measured during longer depolarizing steps (60–80 m), which was unchanged. These findings suggest that clarin-2 is essential for the fast RRP release, but not for the subsequent SRP recruitment. To see whether this defect is due to synaptic machinery abnormalities, we performed UV-flash intracellular $Ca^{2+}$ uncaging experiments to probe exocytosis kinetics independently of $Ca^{2+}$ channels voltage activation (Figure 1F, bottom right). In these conditions, *Clrn2*$^{-/-}$ IHCs displayed a capacitance jump (DCm) with kinetics and maximum amplitudes similar to wild-type IHCs, indicating the presence of a normal pool of RRP vesicles in the active synaptic zones of *Clrn2*$^{-/-}$ IHCs. In conclusion, the progressive hearing loss in *Clrn2*$^{-/-}$ mice not only results from a decrease in MET activity and a regression of the shortest rows of stereocilia of both IHCs and OHCs but is also attributable to a defective spatial organization or abnormal functional coupling of $Ca^{2+}$ channels to synaptic ribbons in *Clrn2*$^{-/-}$ IHCs.

### Development of a virus-mediated gene replacement therapy targeting the Clrn2 deafness gene

We previously showed that the intracochlear administration of AAV8-*Clrn1* to neonatal mice with a *Clrn1* constitutive knockout did not improve their severe hearing loss, presumably because the lack of Clrn1 needed to be corrected earlier in development.[10] Here, we sought to investigate whether virus-mediated transfer of *Clrn2* into hair cells could prevent the structural and functional defects observed in *Clrn2*$^{-/-}$ mice, thereby attenuating hearing loss. We used an AAV9-PHP.eB viral vector and designed a gene therapy construct containing the cytomegalovirus (CMV) promoter, the

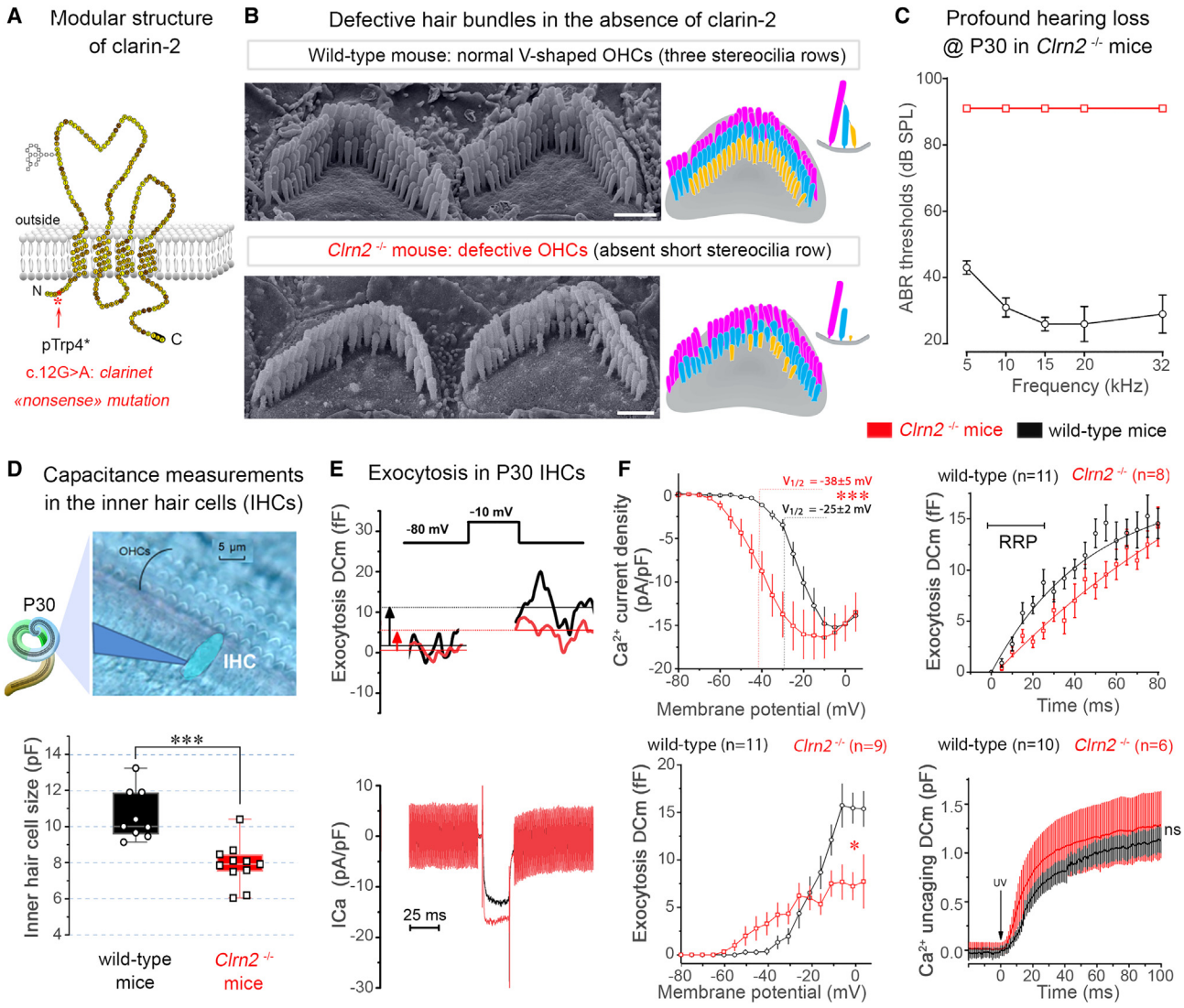


**Figure 1. Lack of clarin-2 leads to profound hearing loss due to hair bundle defects and synaptic dysfunctions**

(A) Structure of clarin-2 protein showing a premature stop codon at position 4 (p.Trp4*) resulting from the c.12G>A variant and leading to complete clarin-2 deficiency in *Clrn2*$^{-/-}$ mice. (B) Scanning electron micrographs of OHC bundles from wild-type and *Clrn2*$^{-/-}$ mice at P30. Almost all the shortest stereocilia have disappeared from the first row of mutant OHC bundles. Scale bar, 1 µm. (C) Measurements of ABR thresholds in P30 wild-type (black) and *Clrn2*$^{-/-}$ (red) mice. ABR threshold elevation in mutant mice (>90 dB SPL) indicates profound hearing loss affecting all frequencies tested. Data represent mean ± SEM from three to six mice per group. (D) Bright-field photomicrograph of a mouse organ of Corti isolated at P30 for whole-cell patch clamp of IHCs. Lower graph shows significantly reduced IHC resting membrane capacitance (resting cell size) in *Clrn2*$^{-/-}$ (red) mice as compared to wild type (black), measured at −70 mV (***p = 0.0002; two-sample t test). (E) Representative examples of exocytosis (DCm) and $Ca^{2+}$ currents ($I_{Ca}$) evoked upon a 25-ms voltage-step stimulation from −80 to −10 mV. (F) Voltage-dependent activation of $Ca^{2+}$ currents (upper left) and exocytosis (lower left) in mutant and wild-type IHCs (***p < 0.0001, *p = 0.025, unpaired t tests for comparative $V_{1/2}$ and Mann-Whitney test for DCm max at 0 mV). Upper right graph shows comparative kinetics of exocytosis, measured after a voltage jump from −80 to −10 mV of increasing duration. Note the significant reduction of the RRP exocytosis component in mutant IHCs (*p < 0.05, Kruskal-Wallis test). Lower right graph shows that exocytosis evoked by intracellular $Ca^{2+}$ uncaging displays normal kinetics (ns, non-significant delays and amplitude, p = 0.9, two-sample t test). Data represent mean ± SEM with n indicating the number of IHCs recorded from four to 11 mice per group.

therapeutic *Clrn2* gene, an IRES-*GFP* sequence, a WPRE sequence, and a 3′ BGH poly(A) sequence (Figure 2A). This construct was packaged into the AAV9-PHP.eB capsid, referred to hereafter as AAV9.eB-*Clrn2*. The expression of the *clarin-2* transgene was confirmed following cell transfection (Figure S2A). We used an equivalent vector lacking the *Clrn2* sequence (AAV9.eB-*GFP*) as a control.

We checked the innocuity of our gene replacement strategy by administering AAV9.eB-*GFP* and AAV9.eB-*Clrn2* in the inner ears

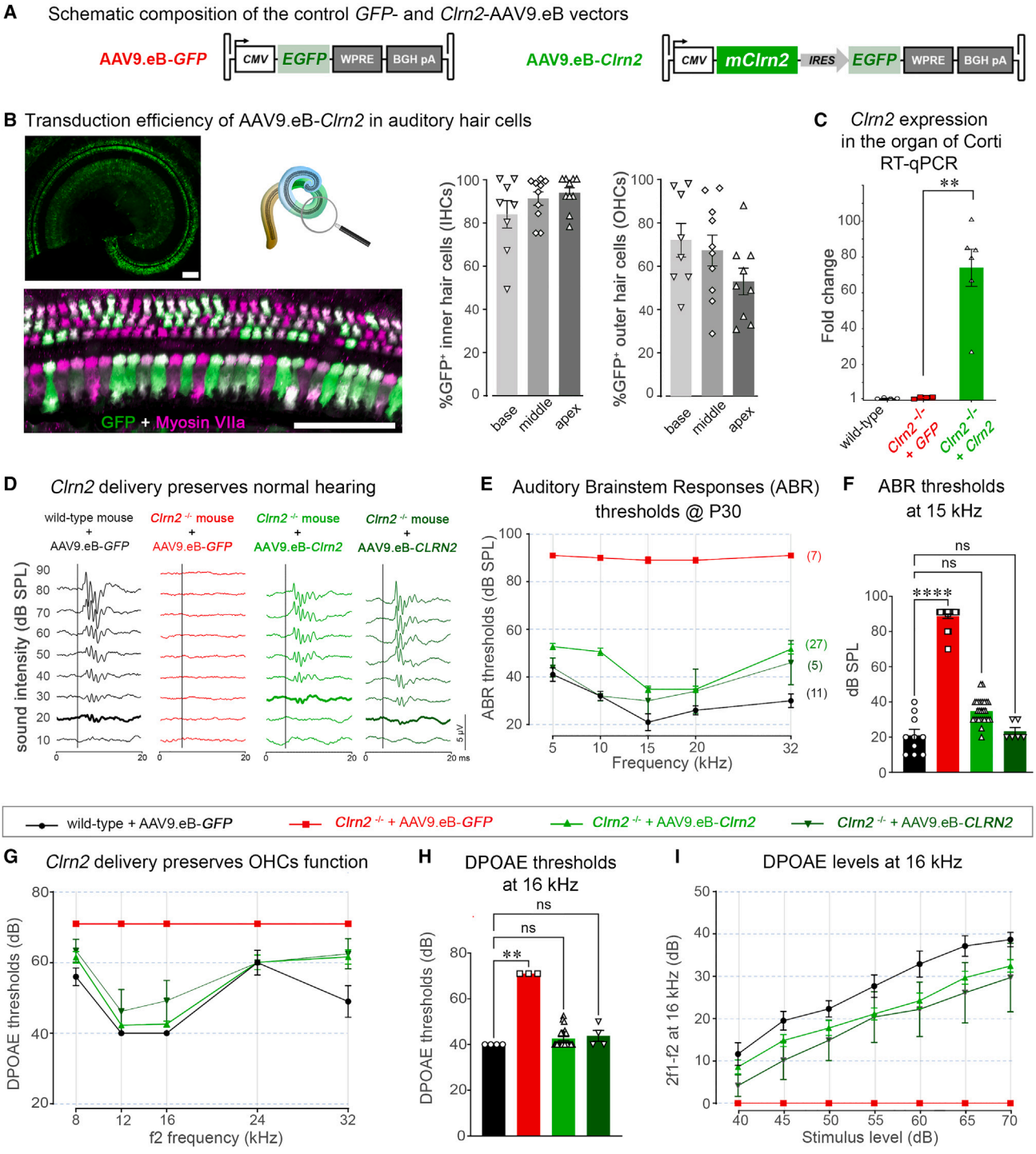


**Figure 2. Neonatal delivery of *Clrn2* leads to successful recovery of hearing**

(A) Schematic diagrams of AAV9.eB-*GFP* and AAV9.eB-*Clrn2* vectors used for gene delivery to the cochlea. Note that both vectors carry a *GFP* cassette. (B) Representative confocal images of the organ of Corti of a P30 *Clrn2*$^{-/-}$ mouse injected at P1 with AAV9.eB-*Clrn2*, showing widespread *GFP* transgene expression (green) from apex to midbase, in Myo7a-positive (magenta) IHCs and OHCs. Scale bars, 100 μm (bottom), 50 μm (top). Histograms of the percentage (mean ± SEM) of GFP-labeled IHCs and OHCs quantified from eight to 10 mice. No significative difference, Kruskal-Wallis tests. (C) mRNA expression levels of the *Clrn2* transgene in organs of Corti of P10 wild-type mice and *Clrn2*$^{-/-}$ mice injected at P1 with AAV9.eB-*GFP* or AAV9.eB-*Clrn2*, showing a more than 70-fold increase in organs of Corti upon injection with AAV9.eB-*Clrn2*.

*(legend continued on next page)*

of neonatal (P1) wild-type mice via injection through the cochlear round window membrane (RWM). These control injections had no significant impact on hearing thresholds for any of the frequencies tested 4 weeks after injection (Figure S2B), demonstrating the safety of our surgical procedure and the innocuity of our AAV vectors. We also checked that administering AAV9.eB-*GFP* to the inner ears of *Clrn2*$^{-/-}$ mice did not affect hearing sensitivity (red curves in Figures S2C and S2D).

We then assessed the efficiency of hair cell transduction with AAV9.eB-*Clrn2*. One month after RWM delivery, the efficiency of IHC transduction (i.e., the percentage of IHCs expressing GFP) was 83% ± 18% at the base of the cochlea, 91% ± 10% at the middle turn, and 94% ± 8% at the apex (Figure 2B). The efficiency of OHC transduction was 72% ± 22% at the base of the cochlea, 67% ± 22% at the middle turn, and 53% ± 18% at the apex (Figure 2B), these rates of OHC transduction being better than those observed with AAV8 vectors.[10] In the three ears with the highest transduction rates, 100% of IHCs and 97% of OHCs were GFP positive. We used real-time RT-qPCR to estimate the levels of *Clrn2* transcripts expressed in the organ of Corti of *Clrn2*$^{-/-}$ mice either injected with AAV9.eB-*GFP* or with AAV9.eB-*Clrn2*, compared to wild-type mice. Ten days after injection, the delivery of AAV9.eB-*Clrn2* at P1 led to a 74 ± 25-fold increase in *Clrn2* transcripts in the hearing organ (Figure 2C). We also performed *in situ* hybridization, which revealed a large number of *Clrn2*-positive mRNA dots in both IHCs and OHCs of AAV9.eB-*Clrn2*-injected *Clrn2*$^{-/-}$ mice (Figure S2E), thus confirming the overexpression of *Clrn2* in hair cells. All these data indicate that AAV9.eB-*Clrn2* can be safely delivered by RWM injections at P1 to efficiently transduce IHCs and OHCs.

### Neonatal delivery of *Clrn2* leads to successful and durable hearing recovery

We assessed the therapeutic potential of *Clrn2* delivery in *Clrn2*$^{-/-}$ mice, by administering either AAV9.eB-*GFP* or AAV9.eB-*Clrn2* to mice via RWM injection at P1 and subsequently evaluated their hearing sensitivity via ABRs at P30. As expected, control AAV9.eB-*GFP* treatment did not prevent deafness in *Clrn2*$^{-/-}$ mice (Figure 2D), which had no recognizable ABR traces across any of the frequencies tested (5–32 kHz) even at sound intensities up to 90 dB sound pressure level (SPL). Conversely, P1 injection of AAV9.eB-*Clrn2* robustly improved hearing sensitivity in *Clrn2*$^{-/-}$ mice across all frequencies tested (Figures 2D–2F), with levels approaching those of wild-type mice (Kruskal-Wallis test). Mean ABR thresholds for AAV9.eB-*Clrn2*-injected *Clrn2*$^{-/-}$ mice with stimuli at 15 kHz were 35 ± 7 dB SPL, whereas corresponding thresholds exceeded 89 ± 6 dB SPL in *Clrn2*$^{-/-}$ mice receiving AAV9.eB-GFP injections (Figures 2E and 2F). An improvement in high-frequency hearing was also observed, with a threshold of almost 50 dB SPL at 32 kHz in *Clrn2*$^{-/-}$ mice that received AAV9.eB-*Clrn2* injections, whereas profound hearing loss (90 dB SPL) was observed in the *Clrn2*$^{-/-}$ mice receiving AAV9.eB-*GFP* injections. Interestingly, seven of the AAV9.eB-*Clrn2* injected *Clrn2*$^{-/-}$ mice displayed ABR thresholds close to those of wild-type mice, with levels rescued to wild type in the two best performers (Figure S2C). Hearing was similarly preserved following delivery of AAV9.eB coding for human *CLRN2*, with ABR thresholds at near-normal values across the 5–32 kHz range (dark green in Figures 2D–2F). Furthermore, measurement of distortion product otoacoustic emissions (DPOAEs) to evaluate cochlear amplification and frequency selectivity showed that all *Clrn2*$^{-/-}$ mice receiving AAV9.eB-*Clrn2* had DPOAE thresholds and levels similar to those of age-matched wild-type mice (Figures 2G–2I) (Kruskal-Wallis test). These findings are consistent with the robust and efficient viral transduction of OHCs observed in treated ears (Figure 2B).

We assessed the durability of the therapeutic effect of AAV9.eB-*Clrn2* on hearing function by conducting monthly follow-up ABR tests up to 6 months after treatment (Figure 3). Hearing sensitivity in AAV9.eB-*Clrn2*-treated *Clrn2*$^{-/-}$ mice was stable over time (Figure 3B). A sustained improvement in ABR thresholds was observed at all tested frequencies between P30 and P180 (Figures 3B and 3C) (Kruskal-Wallis test). Indeed, at the age of six months, the mice in which the intervention was most successful had ABR thresholds that remained close to those of wild-type mice for all frequencies tested in the 5–20 kHz range (Figure S2D). Similarly, longitudinal DPOAE analyses showed a sustained preservation of cochlear OHC function, as illustrated by stable DPOAE thresholds (Figures 3D and 3E) and levels (Figures 3F and 3G) over time.

Together, these findings show that neonatal delivery of AAV9.eB-*Clrn2* durably preserves hearing in *Clrn2*$^{-/-}$ mice across all frequencies tested, as demonstrated by near-normal ABR thresholds and DPOAE measurements obtained up to the age of 6 months.

### Clrn2 delivery maintains the structure and function of hair cell bundles and synapses

We evaluated the morphology of the auditory organ after AAV9.eB-*Clrn2* delivery at P1 by using scanning electron microscopy to assay the sensory epithelia at P30 and P120. In wild-type mice, the auditory organ had a typical checkerboard pattern, with well-organized bundles and visible three rows of stereocilia arranged in staircase formation (Figure S3A). By contrast, at P30, hair bundles in IHCs and OHCs of *GFP*-injected *Clrn2*$^{-/-}$ mice were absent (asterisks in Figures S3B and S3C) or presented alterations to the shortest stereocilia (yellow pseudo-colored in Figures 4A, S3B, and S3C), similar to non-injected *Clrn2*$^{-/-}$ mice.[15] At P30, IHC and OHC bundles of AAV9.eB-*Clrn2*-injected *Clrn2*$^{-/-}$ mice had stereocilia organized in the classic three-row staircase pattern (Figures 4B and S3D). Stereocilia

Data represent mean ± SEM from four to six mice per group. **p < 0.01, Mann-Whitney test. (D–F) Representative ABR waveforms and ABR thresholds of P30 wild-type (black) and *Clrn2*$^{-/-}$ mice injected at P1 with control AAV9.eB-*GFP* (red) or with AAV9.eB vectors coding for murine *Clrn2* (light green) or human *CLRN2* (dark green) genes. At 15 kHz, ABR thresholds of *Clrn2*-treated mice are close to normal values. (G–I) DPOAE thresholds and levels of injected control and mutant mice, showing recovery of OHC function in *Clrn2*-treated mice. Data represent mean ± SEM from 3– 27 mice per group. ****p < 0.0001, **p < 0.01, Kruskal-Wallis tests.

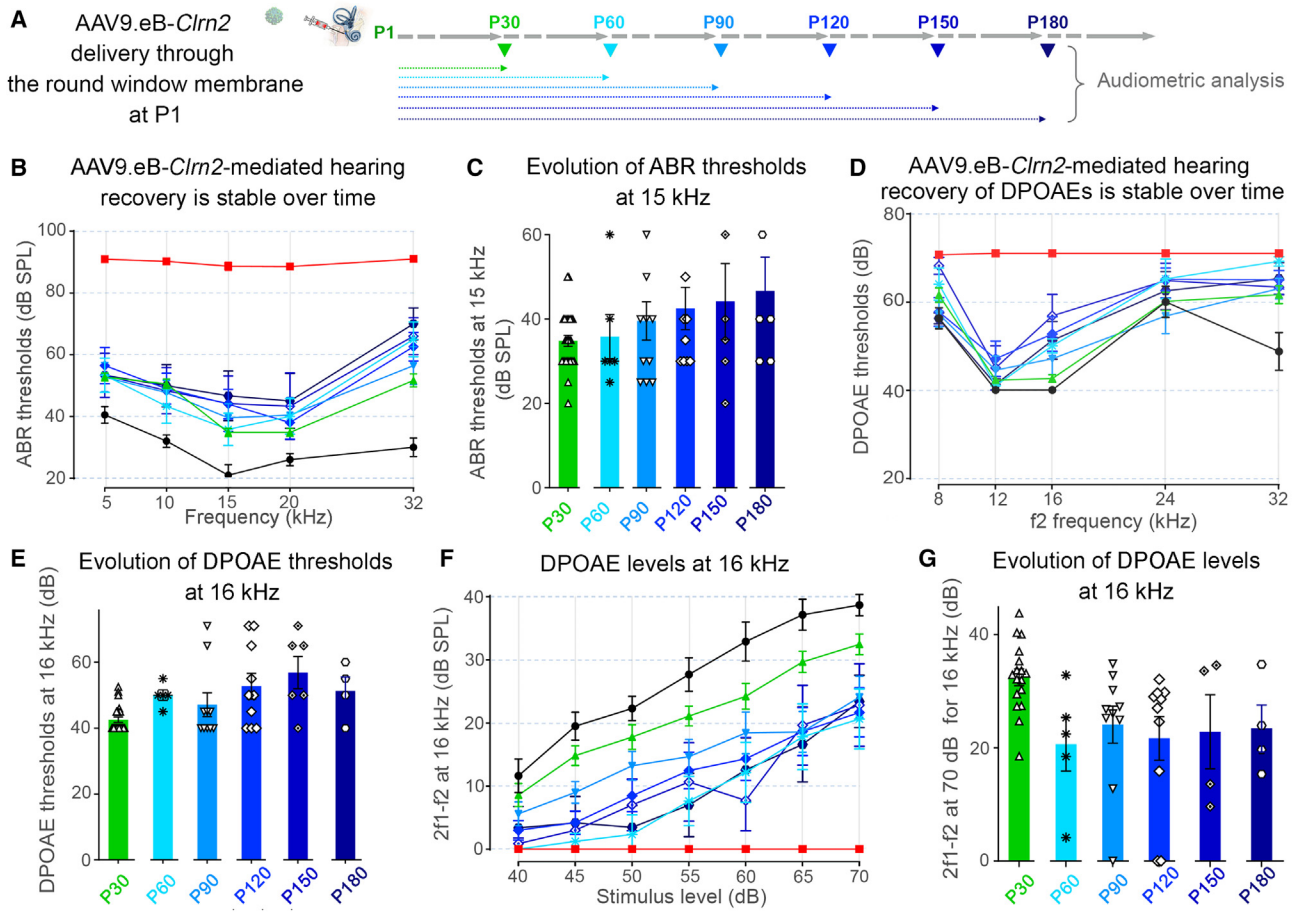


**Figure 3. Neonatal delivery of AAV9.eB-*Clrn2* leads to durable preservation of hearing**

(A) Schematic design of the longitudinal study. (B–G) Audiometric measurements in P30 wild-type (black), P30 *Clrn2*$^{-/-}$ mice injected at P1 with control AAV9.eB-*GFP* (red) and P30 to P180 *Clrn2*$^{-/-}$ mice injected at P1 with AAV9.eB-*Clrn2* (green and blue). ABR (B and C) and DPOAE (D–G) of *Clrn2*-treated mice were measured monthly up to 6 months after injection. Thresholds and levels remain stable with time. Data represent mean ± SEM from 3–27 mice per group. No significative difference, Kruskal-Wallis tests.

rows were organized normally in 55% of OHC bundles in the mid-cochlear turn, consistent with the rate of OHC transduction observed during vector testing (Figure 2B). Counting of shortest (row 3) and tallest (row 1) stereocilia in OHC bundles revealed that the shortest row was well preserved in *Clrn2*-treated *Clrn2*$^{-/-}$ mice (Figure 4C).

We also assessed the cellular preservation of the hearing organ at an adult stage (P120). The lack of clarin-2 in *Clrn2*$^{-/-}$ mice caused a marked degeneration of the sensory epithelium, as illustrated by the loss of almost all hair cells by P120 (Figures 4D and S4A). At this stage, a layer of supporting cells with irregular contours expanded to fill the space normally occupied by auditory hair cells, forming a "flat" epithelium. Only a few occasional hair bundles of IHCs were observed (Figures 4D and S4A). By contrast, in *Clrn2*$^{-/-}$ mice, AAV9.eB-*Clrn2* neonatal injection not only prevented hair cell loss but also preserved the integrity of their hair bundles (Figures 4E, S4B, and S4C), which were similar to those in age-matched wild-type control mice. Shorter stereocilia were missing from some of the OHC bundles in *Clrn2*-treated *Clrn2*$^{-/-}$ mice; these cells were presumed to be non-transduced hair cells lacking *Clrn2* (asterisks in Figures 4E and S4B). However, at P120, most OHC bundles of *Clrn2*-treated *Clrn2*$^{-/-}$ mice displayed a normal organization of stereocilia rows (Figures 4C, 4F, and S4B).

We investigated functional rescue by using FM1-43 fluorescent dye to assess hair cell MET channel activity from post-hearing-onset mature (P30) mice (Figure 5A). FM1-43 was applied away from IHC bundles by a brief pressure puff oriented to deflect them toward the excitatory direction. We then continuously imaged the IHC cuticular plate (where MET channel-bearing stereocilia are anchored) to follow the dynamics of FM1-43 uptake through open MET channels. Consistent with the impairment of MET activity previously demonstrated at an immature postnatal stage (P6),[15] mature P30 IHCs from GFP-injected *Clrn2*$^{-/-}$ mice had lower rates of FM1-43 uptake than IHCs

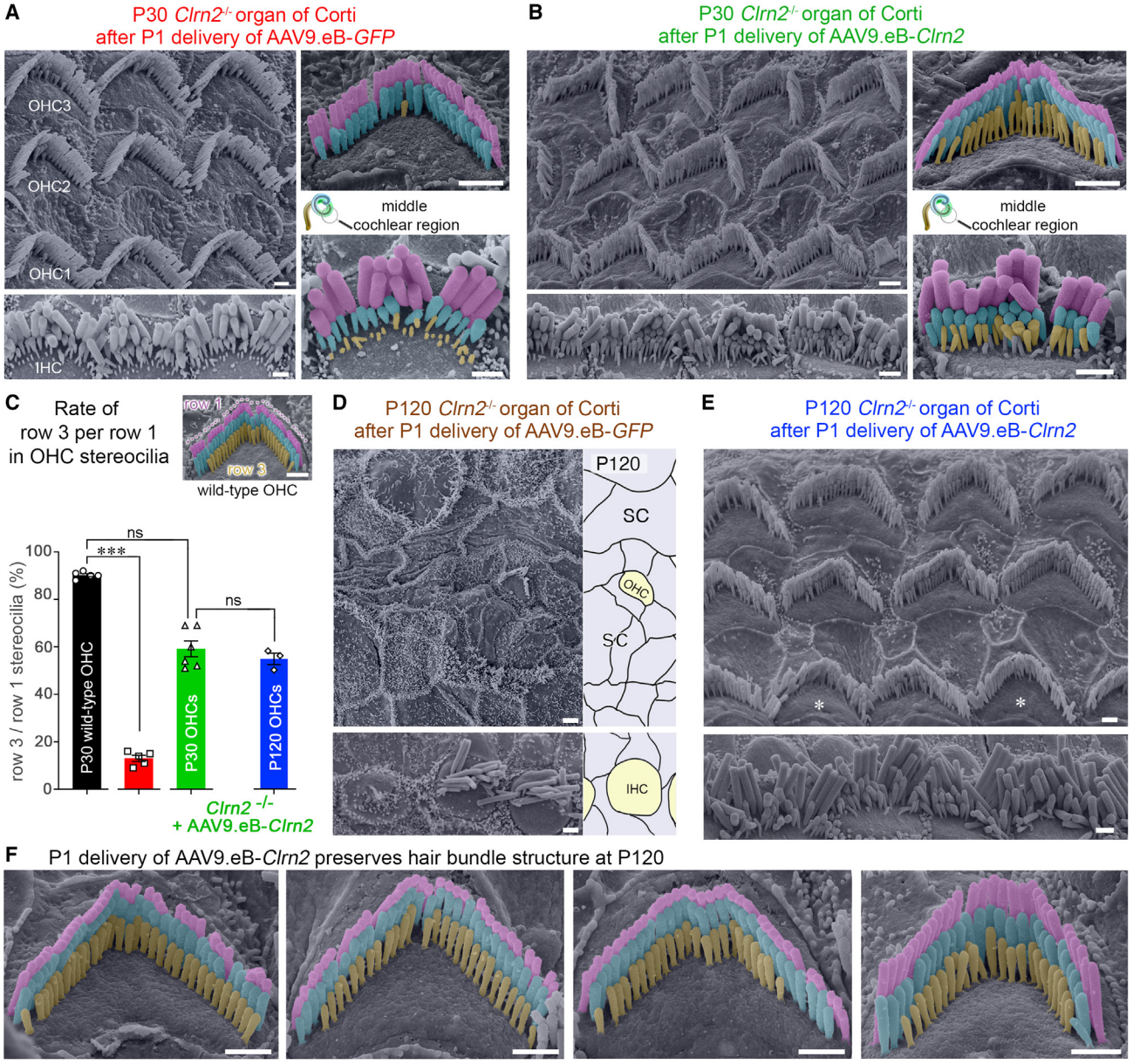


**Figure 4. Neonatal *Clrn2* delivery successfully preserves the hearing organ architecture and stereocilia integrity at P30 and P120**

(A and B) Representative scanning electron micrographs of the sensory epithelium of P30 *Clrn2*$^{-/-}$ mice injected at P1 with AAV9.eB-*GFP* (A) or with AAV9.eB-*Clrn2* (B). Pseudo-colored images of individual IHC and OHC bundles showing that AAV9.eB-*Clrn2* preserves the shortest row of stereocilia (yellow pseudo-colored). (C) Quantification of OHC stereocilia number in wild-type mice (P30, black), *Clrn2*$^{-/-}$ mice injected at P1 with control AAV9.eB-GFP (P30, red), and *Clrn2*$^{-/-}$ mice injected at P1 with AAV.eB-*Clrn2* (P30, green; P120, blue). Ratio of shortest (row 3) to longest (row 1) stereocilia per OHC is improved in *Clrn2*-treated mutant mice. Data represent mean ± SEM from three to six mice per group. ***$p < 0.001$, Kruskal-Wallis test. (D–F) Representative scanning electron micrographs of the sensory epithelium of P120 *Clrn2*$^{-/-}$ mice injected at P1 with AAV9.eB-*GFP* (D) or with AAV9.eB-*Clrn2* (E and F). Pseudo-colored images of individual OHC bundles showing that AAV9.eB-*Clrn2* durably preserves the shortest row of stereocilia (yellow pseudo-colored). Asterisks indicate OHCs with non-corrected shortest row of stereocilia. Scale bars, 1 μm.

from wild-type mice (Figures 5B–5D) ($p = 0.0054$, Mann-Whitney test). Remarkably, P30 IHCs from AAV9.eB-*Clrn2*-treated *Clrn2*$^{-/-}$ mice had a rate of FM1-43 uptake similar to that of age-matched wild-type IHCs (Figures 5B–5D) (Mann-Whitney test). Consistent with these findings, scanning electron microscopy morphological analysis of AAV9.eB-*Clrn2*-treated *Clrn2*$^{-/-}$ mice showed seemingly normal hair bundles with a preservation of the shortest rows of stereocilia in both IHCs and OHCs (Figure 5E). Preserved tip links were visible in IHCs from *Clrn2*-treated *Clrn2*$^{-/-}$ mice (Figure 5E). Furthermore, most IHC and OHC hair bundles had prolate tips,

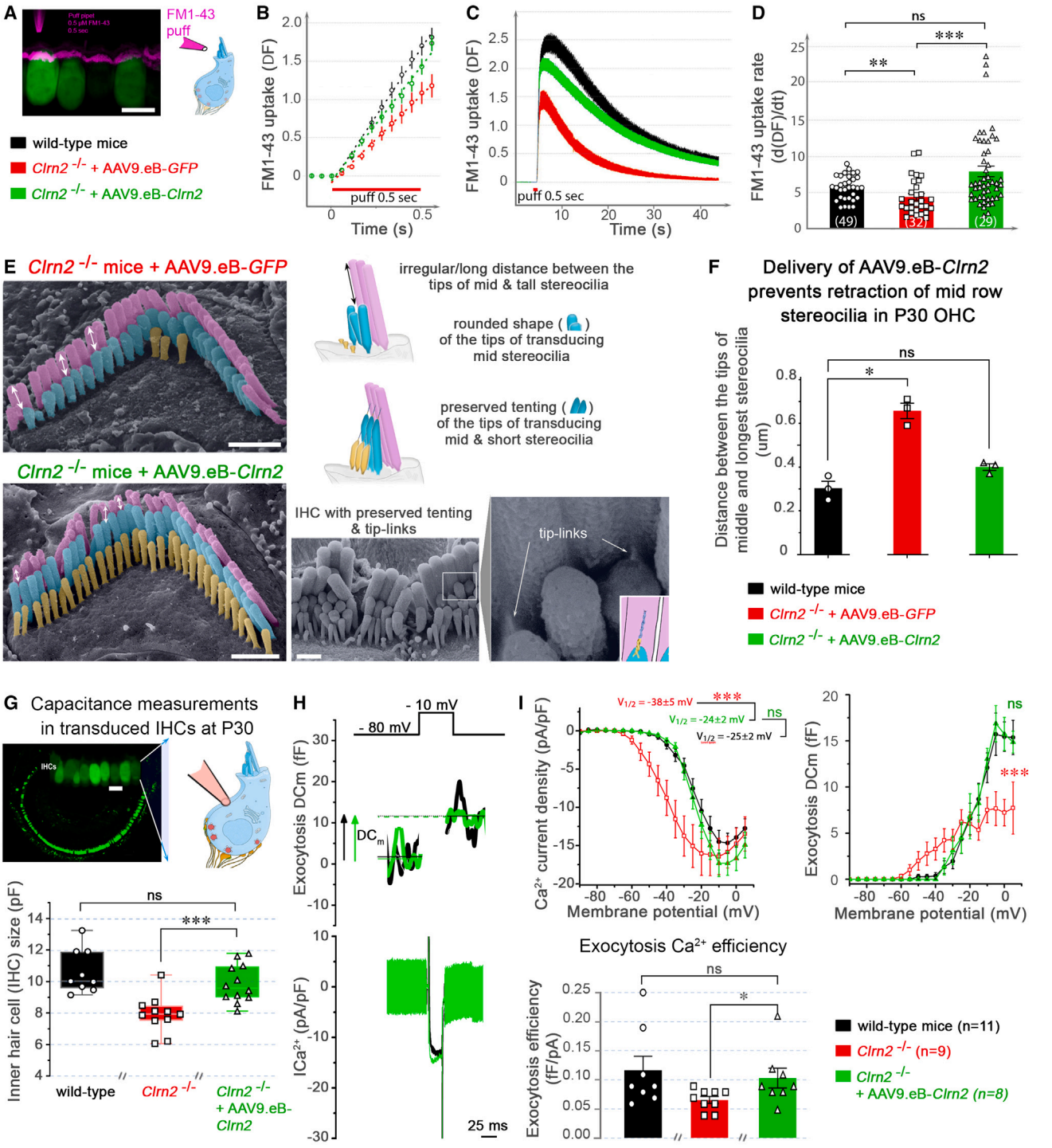


**Figure 5. *Clrn2* delivery successfully preserves structure and function of the hair bundle and the synapse**

(A) Confocal fluorescence imaging of GFP-positive (green) IHCs from a P30 *Clrn2*$^{-/-}$ mouse injected at P1 with AAV9.eB-*Clrn2*. FM1-43 dye (magenta) applied at the apex of IHCs instantaneously entered inside hair bundle stereocilia through open MET channels. Scale bar, 10 μm. (B and C) Comparative kinetics of FM1-43 uptake in wild-type (black) and *Clrn2*$^{-/-}$ mouse injected at P1 with AAV9.eB-*GFP* (red) or with AAV9.eB-*Clrn2* (green). (D) Comparison of the FM1-43 uptake rate after a 0.5-s puff. Data represent mean ± SEM from 29–49 IHCs of three mice per group (ns, p = 0.14; **p = 0.0054, ***p = 0.0001 indicates significance values, Mann-Whitney test). (E) Representative scanning electron micrographs of pseudo-colored OHCs from P30 *Clrn2*$^{-/-}$ mice injected at P1 with AAV9.eB-*GFP* (top) or with AAV9.eB-*Clrn2* (bottom).

*(legend continued on next page)*

so-called tenting, a correlate of functional tip links and active MET channels.[19] Moreover, the "step" distance between the tips of middle (blue pseudo-colored) and tallest (purple pseudo-colored) rows of stereocilia was maintained at normal values in OHCs (Figures 5E and 5F) (Kruskal-Wallis test). Conversely, in *GFP*-injected *Clrn2*$^{-/-}$ mice, OHC bundles had middle-row stereocilia of irregular height with oblate apical wedges (Figure 5E) and a larger step distance between the tips of middle and tallest stereocilia (Figure 5F), indicating MET impairment.

As *Clrn2*$^{-/-}$ mice presented synaptic exocytosis abnormalities associated with hair bundle defects (Figure 1F), we investigated whether these synaptic defects were corrected by AAV-*Clrn2*-mediated gene replacement. IHCs of AAV9.eB-*Clrn2*-treated *Clrn2*$^{-/-}$ mice had a resting cell size similar to that of wild-type IHCs (Figure 5G) (t test). Furthermore, $Ca^{2+}$ currents of IHCs from AAV9.eB-*Clrn2*-treated mice had half-voltage activation levels similar to those of wild-type IHCs (see $V_{1/2}$ values in Figure 5I; t test). Moreover, $Ca^{2+}$ exocytosis efficiency and kinetics in AAV9.eB-*Clrn2*-treated *Clrn2*$^{-/-}$ IHCs were significantly improved (Figure 5I; t test).

Together, our findings confirm the ability of neonatal AAV9.eB-*Clrn2* delivery to compensate effectively for the absence of endogenous Clrn2, preserving both the function and structural features of cochlear hair cell transduction and IHC synaptic features.

### The therapeutic window: Rescue efficiency varies with the age of AAV9.eB-*Clrn2* delivery

Given the progressive postnatal decline of hearing abilities in *Clrn2*$^{-/-}$ mice,[15] we treated mice with the therapeutic vector, AAV9.eB-*Clrn2*, at various postnatal stages to assess the best time window for effective treatment (Figure 6A). Delivery of AAV9.eB-*Clrn2* at P5 resulted in ABR and DPOAE thresholds (purple curves in Figures 6B–6G) close to those achieved upon P1 injections. In the frequency range of 5–20 kHz, *Clrn2*$^{-/-}$ mice treated at P5 had ABR thresholds almost 50 dB SPL lower than those of control *GFP*-injected *Clrn2*$^{-/-}$ mice (Figures 6B and 6C). DPOAE thresholds of *Clrn2*$^{-/-}$ mice treated at P5 were slightly higher than those of *Clrn2*$^{-/-}$ mice treated at P1, but both P1 and P5 deliveries produced significant improvements (Figures 6D–6G). By contrast, in *Clrn2*$^{-/-}$ mice treated with AAV9.eB-*Clrn2* at P10, ABR thresholds at 20 kHz were only 6 dB lower than those of *GFP*-injected *Clrn2*$^{-/-}$ mice (Figure 6B) and displayed no significant improvement in DPOAEs (Figures 6D–6G). *Clrn2*$^{-/-}$ mice injected with AAV9.eB-*Clrn2* at P14 had extremely high ABR and DPOAE thresholds (Figure 6), comparable to those achieved with AAV9.eB-*GFP* injections. Morphological analyses at P30 showed that P5 injection of AAV9.eB-*Clrn2* could still prevent the loss of the shortest stereocilia rows in most of IHCs and OHCs (Figure 7B). By contrast, IHCs and OHCs bundle morphologies in *Clrn2*$^{-/-}$ mice injected at P10 and P14 with AAV9.eB-*Clrn2* (Figures 7C and 7D) were indistinguishable from those of mice receiving AAV9.eB-*GFP*, consistent with the total loss of hearing sensitivity in these mice (Figure 6).

We investigated whether the differences in hearing structural and functional rescues could be attributed to variations of hair cell transduction by quantifying the rate of hair cell transduction after delayed postnatal AAV9.eB-*Clrn2* delivery (Figures 7E and 7F). The percentage of transduced GFP-positive hair cells decreased strongly with increasing age at injection, particularly after P5. For IHCs, the rate of transduction was 90% ± 12% for P1 injections, 87% ± 15% for P5 injections, 79% ± 19% for P10 injections, and 56% ± 26% for P14 injections (Figure 7F). The decrease in transduction efficiency was much more severe for OHCs than for IHCs, decreasing rapidly from 63% ± 29% at P5 (similar to P1) to only 9% ± 15% at P14 (Figure 7F).

Overall, our results demonstrate that the efficiency of hearing rescue in *Clrn2*$^{-/-}$ mice is dependent on interventions occurring within a limited therapeutic time window, with the best results for hearing recovery observed for interventions between P1 and P5, and an extremely poor recovery for interventions occurring at P10 or P14.

### CLRN2 variants in patients and outcome after delivery in Clrn2$^{-/-}$ mouse defective ears

A genetic variant in the human *CLRN2* gene (DFNB117) was recently identified in patients from a consanguineous Iranian family of Lurs ethnicity harboring the c.494C>A variant.[16] Continued analyses of new families with hearing loss allowed us to identify a second unrelated family, also of Lurs ethnicity, with the identical homozygous missense variant (NM_001079827.2: c.494C>A, p.Thr165Lys) in *CLRN2* (Figures 8A and 8B). The variant falls in a 17.8-Mb run of homozygosity on chromosome 4 (Figures S5A and S5B). The proband (II:5, Figure 8A) reported hearing impairment starting around 9–10 years of age, slowly progressing to moderate to severe sensorineural hearing loss when tested at 51 years old (Figure 8B) without subjective

Distance between tips of longest and middle stereocilia (white double arrows), which elongates in mutant mice, is shortened in *Clrn2*-treated mice. Also note the presence of preserved tip links in *Clrn2*-treated IHC (E, bottom panel, white arrows). (F) Measurement of the distance between longest (row 1) and middle (row 2) stereocilia tips. Data represent mean ± SEM from three mice per group. *p < 0.1, Kruskal-Wallis test. Scale bars, 1 μm. (G) Confocal fluorescence imaging of transduced GFP-positive auditory hairs cells in a mouse organ of Corti injected at P1 with AAV.eB-*Clrn2* and isolated at P30 for whole-cell patch clamp of IHCs. Lower graph shows comparative mean IHC resting membrane capacitance (resting cell size) measured at −70 mV, showing reduced size of untreated mutant IHCs (red) and size normalization of Clrn2-treated mutant IHCs (green) compared to wild-type ones (black) (ns, p = 0.91; ***p = 0.0008, two-sample t test). (H) Representative examples of exocytosis (ΔCm) and $Ca^{2+}$ currents (ICa) evoked upon a 25-ms voltage-step stimulation from −80 to −10 mV. (I) Voltage-dependent activation of $Ca^{2+}$ currents (upper left) and associated exocytosis (upper right), as well as maximum exocytosis $Ca^{2+}$ efficiency (lower) in Clrn2-treated mutant (green) IHCs were rescued as compared to wild-type (black) and untreated mutant (red) IHCs: $V_{1/2}$ and maximum exocytosis are similar to wild-type mice, and significantly improved as compared to mutant mice (ns, p = 0.16–0.56; ***p = 0.0005–0.0008, two-sample t test). Data represent mean ± SEM from n = 8 to 12 IHCs of three mice per group.

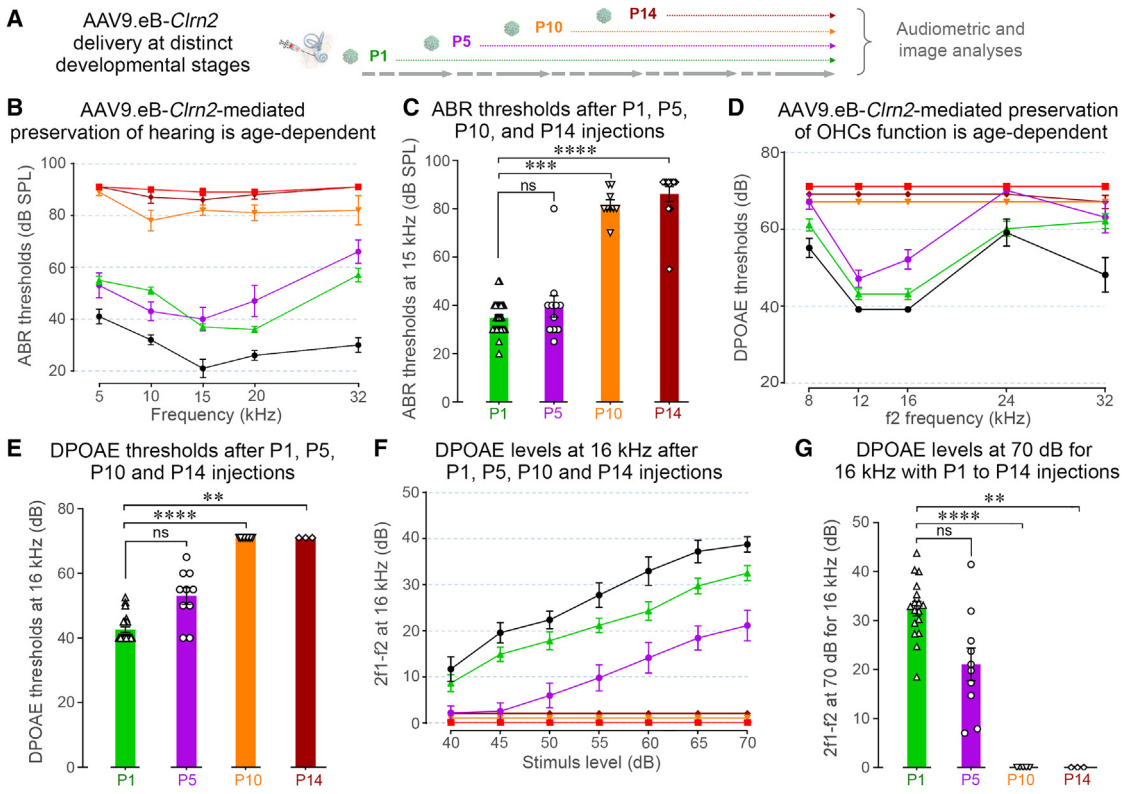


**Figure 6. Preservation of hearing in AAV9.eB-*Clrn2*-treated *Clrn2*$^{-/-}$ mice is age dependent**

(A) Schematic diagram of the experiment design. ABR (B and C) and DPOAE (D–G) of P30 wild-type mice (black), P30 *Clrn2*$^{-/-}$ mice injected at P1 with control AAV9.eB-*GFP* (red) and P30 *Clrn2*$^{-/-}$ mice injected at P1 (green), P5 (purple), P10 (orange), and P14 (dark red) with AAV9.eB-*Clrn2*. Only P1 and P5 injections rescue ABR and DPOAE thresholds, with P1 being more efficient than P5 on DPOAE levels. Data represent mean ± SEM from 3–27 mice per group. **p < 0.01, ***p < 0.001, ****p < 0.0001, Kruskal-Wallis tests.

vestibular or vision impairment. This late onset of hearing impairment in proband II:5 prompted us to revisit the first *CLRN2*-identified family. Through interview with the mother, compared to previous self-reporting,[16] we learned that individuals IV:1 and IV:6 had an onset of hearing impairment at 7 and 10 years, respectively. Together, our findings indicate that *CLRN2* variants are associated with a post-lingual, progressive hearing loss.

Cell-based minigene assays suggested that the *CLRN2* c.494C>A variant could result in two potential transcripts,[16] one leading to a missense substitution in an evolutionary conserved phosphorylation site, p.Thr165Lys (88% of cases) and the other resulting in an abnormally spliced variant retaining an intron and causing a frameshift leading to a premature stop codon (p.Gly146Lysfs*26, hereafter abbreviated *CLRN2*$^{G146Kfs_{\star}26}$, in 12% of cases) (Figure 8C). However, assessments of the pathogenicity of these transcript variants are crucial for accurate diagnosis, prognosis, genetic counseling, and the planning of appropriate interventions. We therefore used our viral rescue approach in *Clrn2*$^{-/-}$ mice and compared therapeutic outcomes in mice treated with AAV9.eB vectors containing the wild-type human *CLRN2* cDNA, AAV9.eB-*CLRN2*$^{T165K}$, or AAV9.eB-*CLRN2*$^{G146Kfs_{\star}26}$. We also injected a mix of AAV9.eB-*CLRN2*$^{T165K}$ (88%) and AAV9.eB-*CLRN2*$^{G146Kfs_{\star}26}$ (12%) to determine whether the combined effect of the two variants was additive. We found that, unlike AAV9.eB-*CLRN2* injection, which maintained near-normal hearing sensitivity, delivery of AAV9.eB-*CLRN2*$^{T165K}$, AAV9.eB-*CLRN2*$^{G146Kfs_{\star}26}$, or both, failed to preserve normal hearing thresholds (Figures 8D and 8E). Consistently, scanning electron microscopy images of OHCs from P30 *Clrn2*$^{-/-}$ mice injected with both mutated forms revealed hair bundles with absent or shortened stereocilia in the transducing short row (Figure 8F). Together, these findings provide clear evidence for the pathogenicity of the *CLRN2* c.494C>A variant and confirm the identification of *CLRN2* as a deafness gene associated with postnatal progressive hearing loss in humans.

## DISCUSSION

This study focused on characterizing the *Clrn2*$^{-/-}$ mouse as a model of progressive hearing loss and evaluating the efficacy of gene therapy for preserving normal hearing. In addition to the previously established effects of clarin-2 loss on hair bundle structure and function,[15] we identified novel phenotypic abnormalities affecting cochlear sensory hair cells and their synaptic function. We demonstrated that neonatal gene supplementation with the murine or human clarin-2

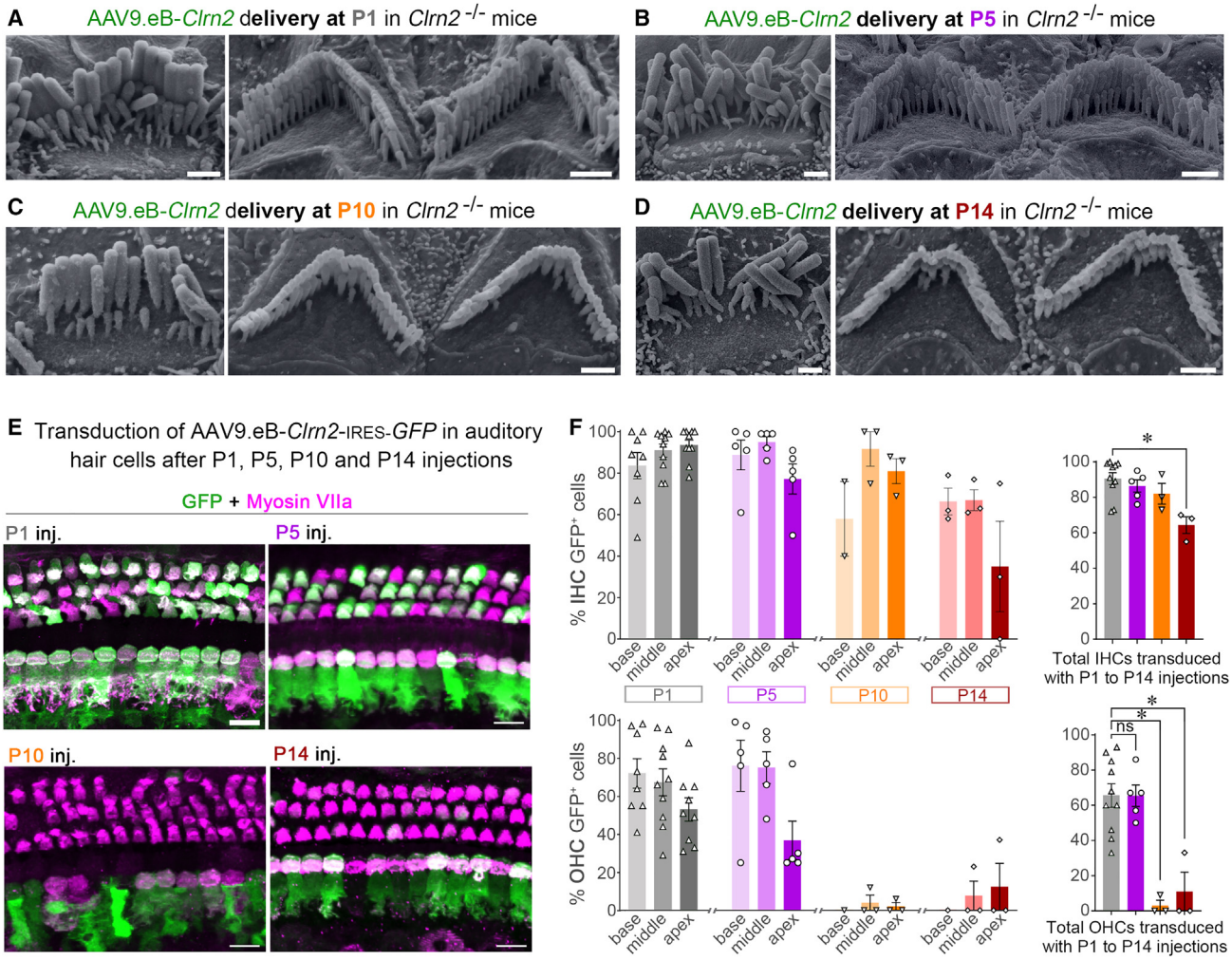


**Figure 7. Delayed delivery of AAV9.eB-*Clrn2* fails to preserve hair bundle integrity**

(A–D) Representative scanning electron micrographs of IHCs and OHCs from P30 *Clrn2*$^{-/-}$ mice injected at P1 (A), P5 (B), P10 (C), and P14 (D) with AAV9.eB-*Clrn2*. Only P1 and P5 injections preserve the shortest row of hair bundle stereocilia. Scale bars, 1 μm. (E) Representative confocal images of Clrn2$^{-/-}$ organs of Corti upon injection with AAV9.eB-*Clrn2*, showing efficient GFP expression (green) in Myo7a-positive (magenta) IHCs at all stages, but absence of GFP expression in OHCs after P10 and P14 injections. Scale bars, 10 μm. (F) Percentage (mean ± SEM) of GFP-labeled IHCs and OHCs quantified from 3–10 mice per group. *p < 0.1, Kruskal-Wallis tests.

gene preserved normal hearing at all frequencies, whereas treatment with mutated variants of *CLRN2* did not. The ectopic expression of *Clrn2* prevented the loss of transducing stereocilia from hair bundles and successfully maintained normal MET and synaptic transmission in auditory hair cells, thereby preserving near-normal hearing over time. Moreover, we confirmed the pathogenicity of *CLRN2* variants identified in patients with progressive hearing impairment.

Our findings demonstrate that functional clarin-2 is required to maintain the well-organized staircase formation of stereocilia in auditory hair cells and proper IHC-to-neuron synaptic transmission. Unlike the Clrn1/Ush3A protein, which is crucial during embryonic development,[10] Clrn2 seems to be crucial at the postnatal stage, consistent with our data showing that Clrn2 levels in hair cells peak by P14.[15] A cross-comparison of synaptic features in the absence of Clrn1[10] and Clrn2 (this study) shows that both proteins are essential for normal synaptic vesicle exocytosis in IHCs. However, unlike in *Clrn1*$^{-/-}$ IHCs, absence of *Clrn2* only affects the fast release of RRP synaptic vesicles, without affecting the exocytotic fusion machinery or the maturation of $Ca^{2+}$ channels in synaptic ribbon active zones. These results suggest that, unlike Clrn1, Clrn2 is not involved in synaptic maturation of $Ca^{2+}$ channels but rather plays an interplay role between $Ca^{2+}$ channel complex and synaptic RRP exocytosis machinery.

Making use of *Clrn2*$^{-/-}$ mice, we assessed the potential of *Clrn2* gene supplementation therapy to rescue the above abnormalities. Multiscale molecular, morphological, functional, and physiological explorations showed that ectopic neonatal expression of *Clrn2* fully

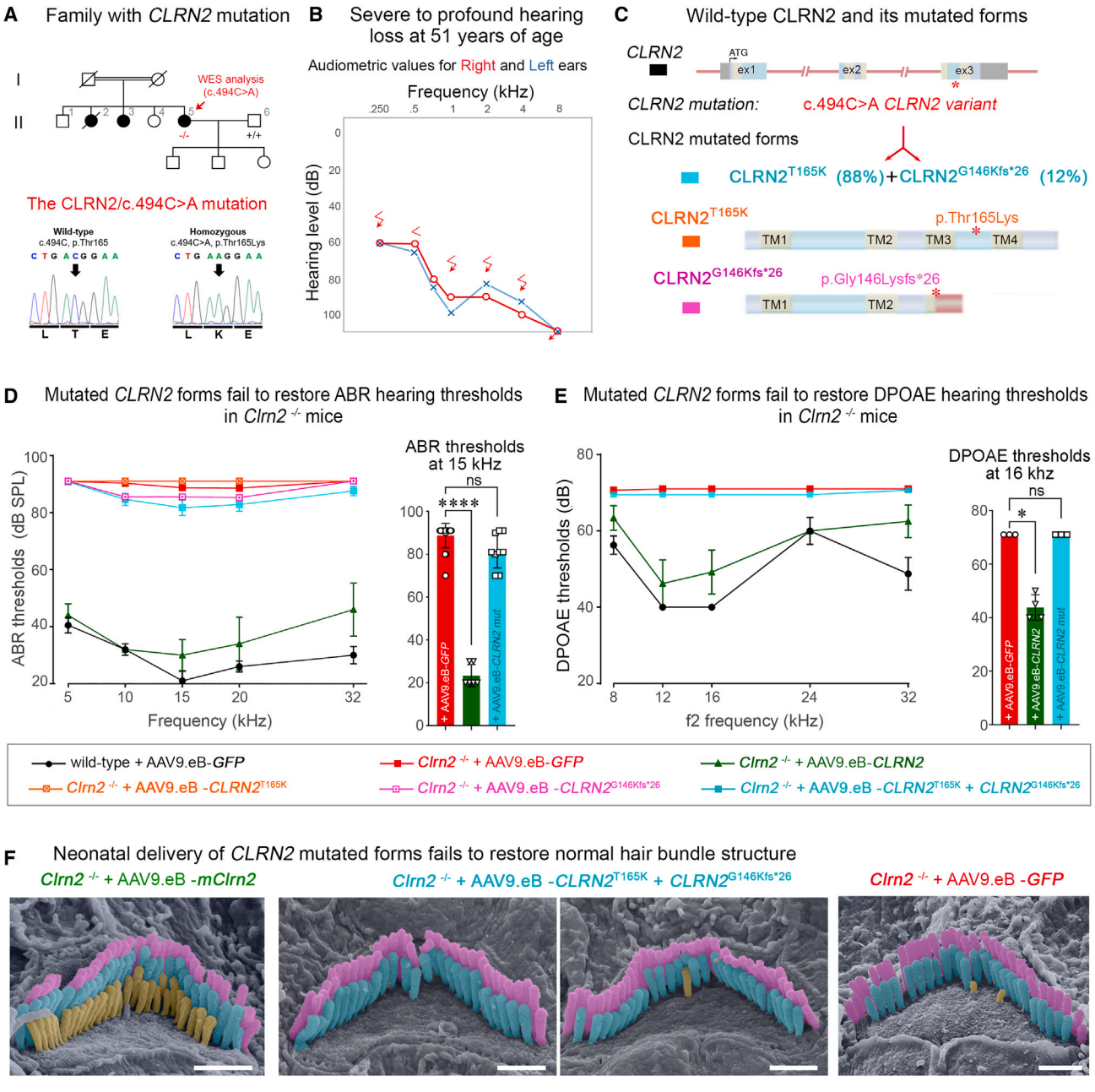


**Figure 8. CLRN2 mutated forms cannot prevent the loss of hearing sensitivity and associated structural deficits**

(A) The pedigree of the family confirming *CLRN2* as a human deafness gene. Sequence electropherograms showing the wild-type sequence (II:6) and homozygous variant (II:5) at position c.494 are shown in the bottom panel. (B) Bilateral pure-tone audiograms from the proband (II:5) at the age of 51 years. Air-conduction thresholds in dB HL for the right (red) and left (blue) ears are shown by circles and crosses, respectively. Bone-conduction thresholds are represented by < and > for right and left ears, respectively, confirming sensorineural hearing loss. (C) Schematic representations of the *CLRN2* gene including the missense mutated allele, c.494C>A, and its two protein variants CLRN2$^{T165K}$ and CLRN2$^{G146Kfs*26}$ resulting from normal (88% of cases) and aberrant (12%) splicing. (D and E) Audiometric measurements in P30 wild-type (black) and *Clrn2*$^{-/-}$ mice injected at P1 with control AAV9.eB-*GFP* (red), AAV9.eB-*CLRN2* (dark green), AAV9.eB-*CLRN2*$^{T165K}$ (orange), AAV9.eB-*CLRN2*$^{G146Kfs*26}$ (magenta), or an 88:12 mix of these last two vectors (AAV9.eB-*CLRN2*$^{mut88:12}$, cyan). None of the mutated *CLRN2* variants can prevent the abnormal elevation of ABR or DPOAE thresholds. Data represent mean ± SEM from 3–19 mice per group. *p < 0.1, ****p < 0.0001, Kruskal-Wallis tests. (F) Representative scanning electron micrographs showing pseudo-colored OHCs from P30 *Clrn2*$^{-/-}$ mice injected at P1 with AAV9.eB-*Clrn2*, a mix of AAV9.eB-*CLRN2*$^{mut88:12}$ or AAV9.eB-*GFP*. *CLRN2* mutated forms fail to preserve the shortest row of OHC bundle stereocilia. Scale bars, 1 μm.

preserved the hearing organ integrity, hair cell bundle arrangement in three stereocilia rows, and normal MET and synaptic IHC functions. The effective prevention of hearing loss in treated *Clrn2*$^{-/-}$ mice contrasts with the very limited and partial rescue of hearing reported for the *Clrn1*,[10,11] *whirlin*,[9] *USH1G*,[8] or *TMC1*[13] genes. This difference in therapeutic outcome can be explained by (1) the robust and efficient delivery of *Clrn2* to most target cells using an improved vector, and (2) gene delivery before irreversible structural abnormalities take place. The AAV9-PHP.B vector, which was first selected for its ability to cross the blood-brain barrier and transduce cells throughout the CNS,[20] was subsequently used in the inner ear for its tropism and efficient transduction of auditory hair cells.[11,21] The AAV9-PHP.eB serotype that we used in the present study is an enhanced variant of AAV9-PHP.B that also transduces most of CNS neurons, but at lower viral load.[22] The CMV promoter and WPRE post-transcriptional regulatory element, used to design our AAV9-PHP.eB vectors, are both known to improve transgene expression in auditory hair cells *in vivo*.[23] Therefore, they likely account for the significant and durable recovery of hearing in *Clrn2*-treated ears, as illustrated by preserved ABRs, DPOAEs, and hearing organ structural integrity for up to 6 months after injection. In terms of safety, a recent study addressed the biodistribution of various AAV subtypes, including AAV9-PHP.B and AAV9-PHP.eB, after intracochlear delivery in neonatal mice, which underscored viral transduction in contralateral inner ear, brain, heart, and liver.[24] Also, intracochlear delivery of AAV9 vectors in non-human primates has been shown to lead to low levels of plasma-circulating anti-AAV9 neutralizing antibodies (Nabs, 1:20–1:40), which did not impede gene transfer in inner ear hair cells, even at doses above $10^{11}$ vector genomes (VGs).[25] Together, these studies stressed the need to measure and compare antibody titers in plasma with those in the perilymph, along with investigations of therapeutic vector biodistribution. To enhance precision of AAV9-PHP.eB vectors, incorporation of specific promoters to govern transgene expression in disease target cells might be pivotal in optimizing the safety profile for intracochlear applications, ensuring sustained efficacy, and minimizing potential risks in translational efforts for hearing restoration.

The lack of clarin-2 led to a severe degeneration of both hair cells and supporting cells in untreated ears. Cuboidal cells with irregular contours expanded to fill the space freed by degenerating hair cells, resulting in the formation of a flat epithelium by P120. Conversely, in treated ears, even hair cells with only two rows of stereocilia (presumably non-transduced cells) remained viable at P120, probably via the stability provided by neighboring transduced healthy hair cells. Thus, even if transduction efficiency is only partial (here about 60% of OHCs), gene therapy can effectively protect the whole hearing organ against the degenerative processes ensuing hearing loss. Such protection could thus be considered to expand further in time the responsiveness of the organ to potential late applications of combinatorial prosthetic and gene therapies.

Unlike neonatal or P5 delivery, which resulted in almost normal hearing by P30, treatment at P10 or P14 failed to prevent *Clrn2*$^{-/-}$ hearing loss. Two non-mutually exclusive hypotheses can account for the gradual loss of therapeutic efficacy upon delayed treatments in *Clrn2*$^{-/-}$ mice: (1) the occurrence of irreversible structural/functional alterations (cf. Figures S1A–S1D;[15]), and (2) a failure to express *Clrn2* in hair cells, due to inefficient transduction at mature stages (cf. Figures 7E and 7F). At an ultrastructural level, organs of Corti of *Clrn2*$^{-/-}$ mice injected at P10/P14 showed no preservation of the short-row stereocilia in both IHCs and OHCs, confirming that treatments beyond P10 are ineffective. Our findings show that, in mice, the P5–P7 period marks a crucial juncture regarding therapy outcomes for key components of the hair bundle (cf. Figures S1A–S1D[15]). The loss of plasticity in stereocilia regrowth may in part explain this critical point of no return. Indeed, hair cells in lower vertebrates can spontaneously regenerate lost stereocilia or hair bundles at mature stages, but mammalian cochlear hair cells have lost this ability.[26,27] Moreover, the presence of an extremely stable F-actin core along the entire stereocilium height[28–30] is not suitable for cellular remodeling, which necessitates cytoskeleton dynamics. During development, hundreds of key proteins operate in precise and intricate choreographed spatiotemporal signaling pathways to enable sequential stereocilium elongation and formation of staircase-arranged hair bundles.[31–35] Impaired MET, such as observed in absence of clarin-2,[15] probably disrupts $Ca^{2+}$ homeostasis, affecting actin polymerization[19,33] and consequently leading to stereocilia regression. Such progressive shortening of transducing stereocilia (rows 2 and 3) has been identified as a hallmark of mice with defects in the MET machinery components (TMC1, TMC2, TMHS/LHFPL5, TMIE, CIB2, CLRN1) (see Vélez-Ortega and Frolenkov[33]). Transducing short-row stereocilia are beginning to regress as early as P6 in *Clrn2*$^{-/-}$ OHCs, while all IHC bundles are normal (see Figures S1A–S1D). These structural changes in stereocilia, evident in OHCs by P6 but not yet in IHCs, likely explain the near-equal levels of ABR thresholds in P1- and P5-treated ears, while a slight (though not yet significant) increase in OHC-related DPOAE thresholds was observed after P5 delivery of *Clrn2* compared to P1 injections. Our findings confirm that, after stereocilia regression (as seen by P10 in *Clrn2*$^{-/-}$ hearing organ[15]), reintroduction of one component of the MET machinery alone, as shown here through addition of clarin-2, would be unable to reactivate the genes and pathways involved in stereociliary elongation and hair bundle morphogenesis, thereby precluding the regrowth of truncated or lost stereocilia. This is consistent with *in vitro* studies using gerbil neonatal hearing organs showing that, after hair bundle ablation, hair cells can survive in culture for up to 2 weeks, displaying signs of functional maturation, but that neither IHCs nor OHCs can repair or regenerate lost stereocilia.[33]

With age, hair cells become refractory to AAV transduction, as attested by the fall in OHCs transduction rate following injection of AAV9.eB-*Clrn2* at P10 and P14, contributing to the poor hearing rescue. Previous studies in mice have also reported a similar age-related decline in transduction efficiency of auditory hair cells with other AAV variants (AAV1, AAV2, Anc80L65, AAV6.2, AAV8, AAV9, AAV9-PHP.B, rh.39, rh.43).[21] Collectively, our findings strongly indicate that two key milestones are crucial for ensuring

the full recovery of hearing: (1) timely intervention before the hearing organ undergoes severe, irreversible structural and functional damages, and (2) the use of vectors with a high rate of transduction into disease target cells at the time of delivery. Delayed treatment, on the other hand, necessitates the development of new AAVs adapted for adult delivery to improve access to mature target cells.

Gene replacement therapy experiments in *Clrn2*$^{-/-}$ mice revealed that, by contrast to what was observed with the wild-type human *CLRN2*, neither hearing sensitivity nor hair bundle structure were preserved after gene supplementation with *CLRN2*$^{T165K}$, harboring a missense substitution, or *CLRN2*$^{G146Kfs*26}$, an abnormally spliced and truncated variant. These findings provide important information for genetic diagnosis and counseling for individuals with genetic variants in *CLRN2*. Thanks to the growing list of disease models, mice will continue to be instrumental in weighing *in vivo* the efficacy of inner ear gene therapies. However, careful attention should be paid not only to interspecies heterochrony but also to differences in disease onset and progression between mice and humans. The rodent inner ear continues to develop and mature during postnatal stages, up to P21, whereas hearing fully develops *in utero* in humans.[36] As such, for most developmental and congenital forms of deafness in humans, resulting in patients being born with severe to profound hearing loss such as Usher syndrome type I,[37–39] the success of potential treatments would probably require *in utero* delivery, before the early embryonic structural disorganization of the developing hair bundle. Nevertheless, there is also growing evidence supporting that, for some deafness causal genes, humans may be more resilient and the therapeutic window can be broader in humans than in mice, at least for several genes. For instance, individuals with *SYNE4* pathogenic variants lead to postnatal progressive hearing loss, more gradual than in *Syne4*$^{-/-}$ mice.[12] Likewise, in USH3A individuals with *CLRN1* pathogenic variants, hearing impairment is progressive and post-lingual, with variable onset, mostly during childhood, but sometimes occurring as late as the age of 35 years.[40] This contrasts with the situation in total *Clrn1*-deficient mice displaying profound hearing loss, with misaligned hair bundles visible at birth.[10,17] For such cases, to extrapolate treatment potential in patients, we suggest prioritizing functional disease indicators and the timeline of patient symptom manifestation (natural history). Functional data (e.g., ABR, DPOAE, language acquisition, speech discrimination) can help infer possible structural correlates, deducing disease stages based on pathogenic metrics from related animal models (mice or others). In the context of *CLRN2*-related disorders, as affected patients all typically develop speech, and hearing problems are post-lingual, manifesting on average beyond 7 years of age, we can assume that hearing is normal during the perinatal period owing to normal mechanoelectrical transduction thanks to still-intact hair bundles. Considering structural-functional correlates, *Clrn2* disease in P1–P7 mice aligns with *CLRN2* symptoms from years 1–7. Consequently, we anticipate that interventions initiated before the loss of mechanoelectrical transduction and the ensuing regression of transducing stereocilia would likely be effective to prevent occurrence of hearing loss. Establishing *Clrn2* models in large animal models (e.g., pig or rabbit), similar to the recent creation of rabbit models with *CLRN1*/Y176X nonsense or N48K missense variants,[41] could better replicate the progressive hearing loss seen in *CLRN*-affected patients. This approach might help confirm the broader therapeutic window and effective outcomes of human-compatible *CLRN2* gene therapies to accelerate clinical translation. Additional data provide further support and expand the potential applicability of *CLRN2*-targeted therapies for age-related hearing impairments. Indeed, with advances in genome analysis techniques and access to large cohorts of participants, such as the UK Biobank, *CLRN2* has been identified among the top-ranking risk genes associated with hearing problems in adults.[15] Multiple recent genome-wide studies in large independent cohorts of patients, including the UK, the Iceland, and the East Europe and America cohorts[18,42–44]) have reported the involvement of *CLRN2* variants in adult hearing difficulties and tinnitus. *CLRN2* variants have also been identified among the list of very rare predicted pathogenic variants causing age-related hearing loss displaying Mendelian inheritance, mARHI.[45] These findings suggest that *CLRN2*-targeted therapies, alone or in combination with therapies targeting other genes for common risk factors, could be broadly applied for age-related hearing impairment, further expanding the list of individuals who would potentially benefit from such an approach.

In summary, the results of this study provide compelling evidence for successful use of gene therapy as a potential treatment for hearing loss. Collectively, our findings demonstrate the feasibility of effective and durable hearing restoration by viral vector-mediated gene therapy in the inner ear of *Clrn2*$^{-/-}$ mice. In mouse studies, *Clrn2* gene therapy demonstrated a capacity to restore near-normal hearing thresholds, presenting a more comprehensive and natural solution compared to the artificial stimulation of cochlear implants. Clinical findings in patients indicate that hearing loss in human patients with *CLRN2* variants may have a later onset and slower progression than in *Clrn2*-deficient mice, broadening the therapeutic window for effective interventions for *CLRN2* genetic disorders. It is thus likely that an early intervention, before symptoms progress, would be key to the complete restoration of hearing function. Overall, this substantial preservation of normal hearing in a model of progressive hearing loss positions gene therapy as a curative solution for profound qualitative improvement in auditory function and marks a significant step forward in the pursuit of auditory restoration.

## MATERIALS AND METHODS

### Study approval

All animal procedures were approved by the Animal Experimentation Ethics Committee (CETEA) of Institut Pasteur and accredited by the French Ministry of Agriculture to allow experiments on live mice (accreditation APAFIS#28758–2020122111365980 v1, issued on 28 December 2020) in appliance of the French and European regulations on care and protection of the Laboratory Animals (Directive 2010/63 EU, French Law 2013-118, 6 February 2013). Protocols were approved by the veterinary staff animal facility and by the biostatistics staff of Institut Pasteur. Human samples were obtained after written informed consent, in accordance with the Declaration of Helsinki and

approved by the local institutional ethics board (no. 3/2/16, University Medical Center Göttingen, Germany).

### Reagents

The full summary of AAV vectors, antibodies, chemicals, medications, and primers is listed in Table S1.

### Mice

C57BL/6J *Clrn2*$^{-/-}$ mice[15] (Clrn2$^{mpc169H}$, MGI: 5792002, MRC Harwell Institute, UK) were backcrossed with the B6-Cdh23c.753G strain[46] (*Cdh23*$^{ahl+em3H}$, MGI: 5749861, MRC Harwell Institute, UK) to eliminate the age-related hearing loss encountered in B6 mice commonly bearing the *Cdh23*c.753A allele. Mice were housed under specific pathogen-free conditions in individually ventilated cages, in a temperature-controlled room, exposed to a 12-h light/dark cycle. Water and food were available *ad libitum*. Male and female mice exhibited similar phenotypes, leading to their grouping together based on genotype.

### Genotyping

Genomic DNA from P5 to P8 toe biopsies was extracted and amplified using the REDExtract-N-Amp Tissue PCR Kit. Targeted regions were PCR amplified using genotyping primers Geno_Cdh23_F/R or Geno_Clrn2_F/R. The PCR products were further treated with Fast AP Thermosensitive Alkaline Phosphatase and *ExoI* Exonuclease before sending to Eurofins Genomics (www.eurofinsgenomics.eu) for Sanger sequencing.

### AVV vectors

Our vectors were designed with the online design platform of VectorBuilder (www.vectorbuilder.com), which also ensured molecular cloning, plasmid DNA preparation, and packaging in AAV9-PHP.eB vectors.

### AAV injection through the RWM

AAV vector micro-injections within the left inner ear of mice were adapted from Emptoz et al.[8] Injections through the RWM were performed under a stereomicroscope (Olympus SZX2-ZB10) on P1–P15 mice anesthetized with isoflurane and placed on a warming pad. A subcutaneous injection of Laocaine was applied locally before skin incision. P10 and P15 mice also received an intraperitoneal injection of buprenorphine 30 min before and 12 h after surgery. P15 animals were shaved on their left peri-auricular zone. At all stages, skin was disinfected with Vetedine solution before incision below the external ear. Soft tissues were pushed apart to expose the otic bulla. Muscle fibers, facial nerve, cochlear basal turn, and stapedial artery were used as landmarks to localize the round window. For P10 and P15 animals, the otic bulla had to be opened to access the RWM. A pulled glass micropipette connected to a silicon tubing linked to a 50-μL Hamilton syringe was used to inject 1 μL of AAV through the RWM. The hole was then plugged with a piece of muscle and the skin was sealed with Vetbond surgical glue. Animals were kept warm until fully awake and then returned to their cages.

### Audiometric tests

Audiometric tests were adapted from a previously described protocol.[10] Mice were anesthetized with an intraperitoneal injection of ketamine and xylazine, and eyes were protected with Ocry-gel. Anesthetized animals were first recorded to collect ABR, and then moved to a second setup to record DPOAE.

#### *ABR recordings and analysis*

Mice were placed into a sound-proof box; three electrodes were subcutaneously positioned on the back (reference), the vertex (negative), and close to the ipsilateral mastoid (positive); and an earpiece speaker was placed at the ear canal entry. Pure sound stimuli were applied at 5, 10, 15, 20, and 32 kHz, from 90 to 10 dB SPL in −10-dB steps. ABR signals were recorded and analyzed with the MATLAB software.

#### *DPOAE recordings and analysis*

Mice were moved to a warming pad and DPOAE recordings were conducted with an OtoPhyLab device piloted by the RT-lab software (Echodia). An eartip, emitting a bitonal acoustic stimulation and recording the resulting eardrum vibrations, was placed at the ear canal entry. Sound stimuli were composed of two tones emitted at two frequencies: f2 (8, 12, 16, 24, and 32 kHz) and f1 (equal to f2/1.20). The intensities of the two tonal stimuli at f1 and f2 were the same, from 70 to 40 dB in −5-dB steps. DPOAE generated at 2f1–f2 were recorded and analyzed. DPOAE thresholds were defined as the weakest stimuli producing a response significantly above the background noise. DPOAE levels having an amplitude of more than 7 dB will be the signature of the presence and functionality of the OHCs.

### Hair cell electrophysiology

Measurements of $Ca^{2+}$ currents and jump in membrane capacitance (ΔCm) in IHCs from wild-type and mutant mice were performed under whole-cell patch-clamp conditions as previously described.[47] Briefly, freshly dissected P30 organs of Corti were placed in a patch-clamp recording chamber containing artificial perilymph with 5 mM $CaCl_2$ at room temperature (RT, 22°C–24°C). Patch pipettes were filled with a cesium-based intracellular solution and recordings were obtained from IHCs placed in the 20%–40% normalized distance from the apex (area coding for frequencies of 8–16 kHz). Resting membrane capacitance (resting cell size) was measured at −70 mV. The voltage dependance of exocytosis (ΔCm) and $Ca^{2+}$ currents (ICa) were simultaneously recorded upon a 25-ms voltage-step stimulation ranging from −80 to −10 mV. The kinetics of release of the RRP and SRP were investigated during a protocol based on constant depolarizing voltage steps from −70 to −10 mV and an increasing step duration from 5 to 80 ms. Exocytosis evoked during intracellular $Ca^{2+}$ uncaging (UV-flash photolysis of DM-nitrophen) was performed under constant voltage-clamp at −80 mV as previously described.[10,48]

### FM1-43 uptake

Freshly dissected P30 organs of Corti were placed in a patch-clamp recording chamber containing artificial perilymph and a patch pipette filled with 0.5 μM FM1-43 fluorescent dye was placed orthogonally at

a distance of 20 μm from IHC hair bundles in order to bend them toward their excitatory direction, i.e., the direction they would follow during excitation, allowing the fluid jet to push the stereocilia from the shortest to the tallest row. Real-time fluorescent confocal images were acquired (18 images/s) before, during, and after a 0.5-s pressure puff of FM1-43, with a C2 confocal microscope (Nikon) piloted by NIS-element imaging software and equipped with a 543-nm helium neon laser system (excitation at 488 nm and emission at >640 nm, Melles Griot 05-LGR-193-381). Fluorescence emission was subsequently measured with ImageJ software by drawing a region of interest focused at the anchoring point of stereocilia in the cuticular plate.

#### Immunofluorescence and confocal imaging

Immunofluorescent staining was adapted from a previously described protocol.[10] Mice were euthanized 30 days after AAV injection and inner ears taken out from the skull. For each ear, the posterior semi-circular canal was cut, and a tiny hole was made at the apex of the cochlea. Ears were then fixed in 4% paraformaldehyde (PFA) diluted in DPBS for 1 h at RT and decalcified in 0.5M ethylenediaminetetraacetic acid (EDTA) overnight at 4°C. After three washes in DPBS, organs of Corti were micro-dissected before permeabilization and saturation for 1 h at RT in DPBS 1% bovine serum albumin (BSA) 0.5% Triton X-100. Samples were then incubated overnight at 4°C with goat anti-GFP conjugated to DyLight488 and rabbit anti-Myosin VIIa diluted in DPBS 1% BSA. After three washes in DPBS, tissues were incubated for 2 h at RT with anti-rabbit antibody conjugated to Alexa Fluor 555 and Hoechst nuclear dye diluted in DPBS 1% BSA. Washed organs of Corti were then mounted in FluoromountG. Background of all fluorescence signals was verified by staining samples with the appropriate secondary antibody alone and with unstained sample controls. Images were captured with an A1R confocal microscope piloted by the NIS-elements imaging software (Nikon). The z stacks of organs of Corti were imaged with a 40× silicon immersion objective. Detectors were set to detect an optimal signal below saturation limits and staining panels were acquired during the same session using identical acquisition settings. Three-dimensional volume images were used to count Myosin VIIa-positive IHCs and OHCs. Among these cells, GFP-positive cells were counted to finally express the percentage of AAV-transduced IHCs and OHCs.

#### Scanning electron microscopy

Sample preparation for scanning electron microscopy was adapted from a previously described protocol.[15] Peri-auricular regions were quickly extracted from P30 or P120 mice and a small hole was made in the apex of the cochlea. Samples were fixed in 2.5% glutaraldehyde diluted in 0.1 M sodium cacodylate (pH 7.4) for 2 h at RT before an overnight decalcification at 4°C in 0.35 M EDTA diluted in 0.75% glutaraldehyde, followed by a 2-h postfixation in 2.5% glutaraldehyde at RT. After three washes in DPBS, organs of Corti were micro-dissected, washed in 0.1 M sodium cacodylate, and then processed with the OTOTO protocol consisting of three incubations of 30 min at RT with 1% tetroxide osmium diluted in 0.1 M sodium cacodylate alternated with two incubations of 15 min at RT with 0.1 M thiocarbohydrazide. Each of these five steps was separated by six washes in ultrapure water. Samples were then dehydrated through a graded ethanol series (50%, 70%, 85%, 95%, 100%, 5 min each) followed by 15 min in hexamethyldisilazane and air drying. Samples were then mounted on carbon film glued to aluminum stubs (Oxford Instruments) and coated with gold/palladium using a Quorum Q150R S sputter coater (Quorum Technologies). Scanning images were acquired with a JEOL IT700HR scanning electron microscope. Counting of shortest (row 3) and longest (row 1) OHC bundle stereocilia and distance measurement between longest (row 1) and middle (row 2) OHC stereocilia were performed with the graphic tools of ZEN lite free software (www.zeiss.com).

#### Patient recruitment, clinical examination, and exome sequencing

Written informed consent was provided from participating individuals. Individual II:5 underwent ear, nose, and throat examination and underwent routine pure-tone audiometry according to current standards. Exome sequencing of the DNA from individual II:5 and variant filtering were performed as previously described.[16] Regions of homozygosity were calculated by imputing the proband exome dataset into AutoMap.[49]

#### Statistics

Statistical analyses were performed using Prism 9 (GraphPad). Tests utilized for comparison of two datasets were unpaired t test when data met normal distribution and Mann-Whitney test otherwise. Tests utilized for comparison of three or more datasets were ordinary one-way or two-way ANOVA when data met normal distribution and Kruskal-Wallis test otherwise. p values <0.1 were considered significant. Sample size and additional details are provided in the figure legends.

## DATA AND CODE AVAILABILITY

The data that support the findings of this study are available from the corresponding author, A.E., upon reasonable request.

## SUPPLEMENTAL INFORMATION

Supplemental information can be found online at https://doi.org/10.1016/j.ymthe.2024.01.021.

## ACKNOWLEDGMENTS

The work in the authors' laboratories is funded by the French National Research Agency (ANR) as part of the second Investissements d'Avenir program (Light4deaf, ANR-15-RHUS-0001), ANR-Hear-InNoise (ANR-17-CE16-0017), EuroNanoMed-NanoEar (ANR-21-ENM3-0003-04), Fondation Voir et Entendre, Fondation de France, Fondation Pour l'Audition (FPA-19-Stg), and the Foundation Fighting Blindness (PPA-0922-0840-INSERM) to A.E.; the German Research Foundation DFG (VO 2138/7-1 grant 469177153) to B.V.; and the Medical Research Council (MR/X004597/1) to M.R.B. C.M. benefited from IP-SU PhD fellowship and P.P. from the European-Union's-Horizon 2020 Marie Sklodowska-Curie (grant N°665807). We acknowledge the support provided to the Institut de l'Audition by Fondation pour l'Audition. We thank Maia Brunstein of the

Bioimaging Core Facility, Clara Dussaux of the Data Acquisition and Neural Signal Processing Facility, and Adeline Mallet and Christine Schmitt of the Ultrastructural Bioimaging Facility for their help in image acquisition and data analysis. The JEOL IT700HR scanning electron microscope was funded by the French government (ANR-10-LABX-62-IBEID). Graphical abstract was created with BioRender.com.

## AUTHOR CONTRIBUTIONS

C.M., C.F., and S.V. performed injections, audiometric tests, histology, immunostaining, and imaging. T.P. and D.D. performed and analyzed electrophysiological recordings. S.P. performed western blots. N.Y. and P.P. contributed sample preparation. S.N. performed mouse genotyping. S.V. performed RNAscope and RT-PCR. M.Z., N.C., R.M., H.G., and B.V. contributed study samples and clinical data. M.R.B., A.M., D.D., and S.D. provided biological materials and scientific input and gave feedback on the manuscript. A.E. and S.V. designed the study and wrote the manuscript.

## DECLARATION OF INTERESTS

The authors declare no competing interests.

## REFERENCES

1. Delmaghani, S., and El-Amraoui, A. (2020). Inner Ear Gene Therapies Take Off: Current Promises and Future Challenges. J. Clin. Med. *9*, 2309. https://doi.org/10.3390/jcm9072309.

2. McDaid, D., Park, A.L., and Chadha, S. (2021). Estimating the global costs of hearing loss. Int. J. Audiol. *60*, 162–170. https://doi.org/10.1080/14992027.2021.1883197.

3. Taiber, S., Gwilliam, K., Hertzano, R., and Avraham, K.B. (2022). The Genomics of Auditory Function and Disease. Annu. Rev. Genomics Hum. Genet. *23*, 275–299. https://doi.org/10.1146/annurev-genom-121321-094136.

4. Livingston, G., Huntley, J., Sommerlad, A., Ames, D., Ballard, C., Banerjee, S., Brayne, C., Burns, A., Cohen-Mansfield, J., Cooper, C., et al. (2020). Dementia prevention, intervention, and care: 2020 report of the Lancet Commission. Lancet *396*, 413–446. https://doi.org/10.1016/S0140-6736(20)30367-6.

5. Wolf, B.J., Kusch, K., Hunniford, V., Vona, B., Kühler, R., Keppeler, D., Strenzke, N., and Moser, T. (2022). Is there an unmet medical need for improved hearing restoration? EMBO Mol. Med. *14*, e15798. https://doi.org/10.15252/emmm.202215798.

6. Carlyon, R.P., and Goehring, T. (2021). Cochlear Implant Research and Development in the Twenty-first Century: A Critical Update. J. Assoc. Res. Otolaryngol. *22*, 481–508. https://doi.org/10.1007/s10162-021-00811-5.

7. Askew, C., and Chien, W.W. (2020). Adeno-associated virus gene replacement for recessive inner ear dysfunction: Progress and challenges. Hear. Res. *394*, 107947. https://doi.org/10.1016/j.heares.2020.107947.

8. Emptoz, A., Michel, V., Lelli, A., Akil, O., Boutet de Monvel, J., Lahlou, G., Meyer, A., Dupont, T., Nouaille, S., Ey, E., et al. (2017). Local gene therapy durably restores vestibular function in a mouse model of Usher syndrome type 1G. Proc. Natl. Acad. Sci. USA *114*, 9695–9700. https://doi.org/10.1073/pnas.1708894114.

9. Isgrig, K., Shteamer, J.W., Belyantseva, I.A., Drummond, M.C., Fitzgerald, T.S., Vijayakumar, S., Jones, S.M., Griffith, A.J., Friedman, T.B., Cunningham, L.L., and Chien, W.W. (2017). Gene Therapy Restores Balance and Auditory Functions in a Mouse Model of Usher Syndrome. Mol. Ther. *25*, 780–791. https://doi.org/10.1016/j.ymthe.2017.01.007.

10. Dulon, D., Papal, S., Patni, P., Cortese, M., Vincent, P.F., Tertrais, M., Emptoz, A., Tlili, A., Bouleau, Y., Michel, V., et al. (2018). Clarin-1 gene transfer rescues auditory synaptopathy in model of Usher syndrome. J. Clin. Invest. *128*, 3382–3401. https://doi.org/10.1172/JCI94351.

11. György, B., Meijer, E.J., Ivanchenko, M.V., Tenneson, K., Emond, F., Hanlon, K.S., Indzhykulian, A.A., Volak, A., Karavitaki, K.D., Tamvakologos, P.I., et al. (2019). Gene Transfer with AAV9-PHP.B Rescues Hearing in a Mouse Model of Usher Syndrome 3A and Transduces Hair Cells in a Non-human Primate. Mol. Ther. Methods Clin. Dev. *13*, 1–13. https://doi.org/10.1016/j.omtm.2018.11.003.

12. Taiber, S., Cohen, R., Yizhar-Barnea, O., Sprinzak, D., Holt, J.R., and Avraham, K.B. (2021). Neonatal AAV gene therapy rescues hearing in a mouse model of SYNE4 deafness. EMBO Mol. Med. *13*, e13259. https://doi.org/10.15252/emmm.202013259.

13. Wu, J., Solanes, P., Nist-Lund, C., Spataro, S., Shubina-Oleinik, O., Marcovich, I., Goldberg, H., Schneider, B.L., and Holt, J.R. (2021). Single and Dual Vector Gene Therapy with AAV9-PHP.B Rescues Hearing in Tmc1 Mutant Mice. Mol. Ther. *29*, 973–988. https://doi.org/10.1016/j.ymthe.2020.11.016.

14. Askew, C., Rochat, C., Pan, B., Asai, Y., Ahmed, H., Child, E., Schneider, B.L., Aebischer, P., and Holt, J.R. (2015). Tmc gene therapy restores auditory function in deaf mice. Sci. Transl. Med. *7*, 295ra108. https://doi.org/10.1126/scitranslmed.aab1996.

15. Dunbar, L.A., Patni, P., Aguilar, C., Mburu, P., Corns, L., Wells, H.R., Delmaghani, S., Parker, A., Johnson, S., Williams, D., et al. (2019). Clarin-2 is essential for hearing by maintaining stereocilia integrity and function. EMBO Mol. Med. *11*, e10288. https://doi.org/10.15252/emmm.201910288.

16. Vona, B., Mazaheri, N., Lin, S.J., Dunbar, L.A., Maroofian, R., Azaiez, H., Booth, K.T., Vitry, S., Rad, A., Rüschendorf, F., et al. (2021). A biallelic variant in CLRN2 causes non-syndromic hearing loss in humans. Hum. Genet. *140*, 915–931. https://doi.org/10.1007/s00439-020-02254-z.

17. Geng, R., Melki, S., Chen, D.H.C., Tian, G., Furness, D.N., Oshima-Takago, T., Neef, J., Moser, T., Askew, C., Horwitz, G., et al. (2012). The mechanosensory structure of the hair cell requires clarin-1, a protein encoded by Usher syndrome III causative gene. J. Neurosci. *32*, 9485–9498. https://doi.org/10.1523/jneurosci.0311-12.2012.

18. Wells, H.R.R., Freidin, M.B., Zainul Abidin, F.N., Payton, A., Dawes, P., Munro, K.J., Morton, C.C., Moore, D.R., Dawson, S.J., and Williams, F.M.K. (2019). GWAS Identifies 44 Independent Associated Genomic Loci for Self-Reported Adult Hearing Difficulty in UK Biobank. Am. J. Hum. Genet. *105*, 788–802. https://doi.org/10.1016/j.ajhg.2019.09.008.

19. Vélez-Ortega, A.C., Freeman, M.J., Indzhykulian, A.A., Grossheim, J.M., and Frolenkov, G.I. (2017). Mechanotransduction current is essential for stability of the transducing stereocilia in mammalian auditory hair cells. Elife *6*, e24661. https://doi.org/10.7554/eLife.24661.

20. Deverman, B.E., Pravdo, P.L., Simpson, B.P., Kumar, S.R., Chan, K.Y., Banerjee, A., Wu, W.L., Yang, B., Huber, N., Pasca, S.P., and Gradinaru, V. (2016). Cre-dependent selection yields AAV variants for widespread gene transfer to the adult brain. Nat. Biotechnol. *34*, 204–209. https://doi.org/10.1038/nbt.3440.

21. Lee, J., Nist-Lund, C., Solanes, P., Goldberg, H., Wu, J., Pan, B., Schneider, B.L., and Holt, J.R. (2020). Efficient viral transduction in mouse inner ear hair cells with utricle injection and AAV9-PHP. Hear. Res. *394*, 107882. https://doi.org/10.1016/j.heares.2020.107882.

22. Chan, K.Y., Jang, M.J., Yoo, B.B., Greenbaum, A., Ravi, N., Wu, W.L., Sánchez-Guardado, L., Lois, C., Mazmanian, S.K., Deverman, B.E., and Gradinaru, V. (2017). Engineered AAVs for efficient noninvasive gene delivery to the central and peripheral nervous systems. Nat. Neurosci. *20*, 1172–1179. https://doi.org/10.1038/nn.4593.

23. Marcovich, I., Baer, N.K., Shubina-Oleinik, O., Eclov, R., Beard, C.W., and Holt, J.R. (2022). Optimized AAV Vectors for TMC1 Gene Therapy in a Humanized Mouse Model of DFNB7/11. Biomolecules *12*, 914. https://doi.org/10.3390/biom12070914.

24. Han, S., Xu, Z., Wang, S., Tang, H., Hu, S., Wang, H., Guan, G., and Shu, Y. (2023). Distributional comparison of different AAV vectors after unilateral cochlear administration. Gene Ther. https://doi.org/10.1038/s41434-023-00431-z.

25. Ivanchenko, M.V., Hanlon, K.S., Devine, M.K., Tenneson, K., Emond, F., Lafond, J.F., Kenna, M.A., Corey, D.P., and Maguire, C.A. (2020). Preclinical testing of AAV9-PHP.B for transgene expression in the non-human primate cochlea. Hear. Res. *394*, 107930. https://doi.org/10.1016/j.heares.2020.107930.

26. Burns, J.C., and Corwin, J.T. (2013). A historical to present-day account of efforts to answer the question: "what puts the brakes on mammalian hair cell regeneration?". Hear. Res. *297*, 52–67. https://doi.org/10.1016/j.heares.2013.01.005.

27. Maudoux, A., Vitry, S., and El-Amraoui, A. (2022). Vestibular deficits in deafness: clinical presentation, animal modeling and treatment solutions. Front. Neurol. *13*, 816534. https://doi.org/10.3389/fneur.2022.816534.

28. Zhang, D.S., Piazza, V., Perrin, B.J., Rzadzinska, A.K., Poczatek, J.C., Wang, M., Prosser, H.M., Ervasti, J.M., Corey, D.P., and Lechene, C.P. (2012). Multi-isotope imaging mass spectrometry reveals slow protein turnover in hair-cell stereocilia. Nature *481*, 520–524. https://doi.org/10.1038/nature10745.

29. Drummond, M.C., Barzik, M., Bird, J.E., Zhang, D.S., Lechene, C.P., Corey, D.P., Cunningham, L.L., and Friedman, T.B. (2015). Live-cell imaging of actin dynamics reveals mechanisms of stereocilia length regulation in the inner ear. Nat. Commun. *6*, 6873. https://doi.org/10.1038/ncomms7873.

30. Narayanan, P., Chatterton, P., Ikeda, A., Ikeda, S., Corey, D.P., Ervasti, J.M., and Perrin, B.J. (2015). Length regulation of mechanosensitive stereocilia depends on very slow actin dynamics and filament-severing proteins. Nat. Commun. *6*, 6855. https://doi.org/10.1038/ncomms7855.

31. Tilney, L.G., Tilney, M.S., and DeRosier, D.J. (1992). Actin filaments, stereocilia, and hair cells: how cells count and measure. Annu. Rev. Cell Biol. *8*, 257–274. https://doi.org/10.1146/annurev.cb.08.110192.001353.

32. McGrath, J., Roy, P., and Perrin, B.J. (2017). Stereocilia morphogenesis and maintenance through regulation of actin stability. Semin. Cell Dev. Biol. *65*, 88–95. https://doi.org/10.1016/j.semcdb.2016.08.017.

33. Vélez-Ortega, A.C., and Frolenkov, G.I. (2019). Building and repairing the stereocilia cytoskeleton in mammalian auditory hair cells. Hear. Res. *376*, 47–57. https://doi.org/10.1016/j.heares.2018.12.012.

34. Wagner, E.L., and Shin, J.B. (2019). Mechanisms of Hair Cell Damage and Repair. Trends Neurosci. *42*, 414–424. https://doi.org/10.1016/j.tins.2019.03.006.

35. Krey, J.F., and Barr-Gillespie, P.G. (2019). Molecular Composition of Vestibular Hair Bundles. Cold Spring Harb. Perspect. Med. *9*, a033209. https://doi.org/10.1101/cshperspect.a033209.

36. Hall, J.W., 3rd (2000). Development of the ear and hearing. J. Perinatol. *20*, S12–S20. https://doi.org/10.1038/sj.jp.7200439.

37. Lefèvre, G., Michel, V., Weil, D., Lepelletier, L., Bizard, E., Wolfrum, U., Hardelin, J.P., and Petit, C. (2008). A core cochlear phenotype in USH1 mouse mutants implicates fibrous links of the hair bundle in its cohesion, orientation and differential growth. Development *135*, 1427–1437. https://doi.org/10.1242/dev.012922.

38. Géléoc, G.G.S., and El-Amraoui, A. (2020). Disease mechanisms and gene therapy for Usher syndrome. Hear. Res. *394*, 107932. https://doi.org/10.1016/j.heares.2020.107932.

39. Delmaghani, S., and El-Amraoui, A. (2022). The genetic and phenotypic landscapes of Usher syndrome: from disease mechanisms to a new classification. Hum. Genet. *141*, 709–735. https://doi.org/10.1007/s00439-022-02448-7.

40. Ness, S.L., Ben-Yosef, T., Bar-Lev, A., Madeo, A.C., Brewer, C.C., Avraham, K.B., Kornreich, R., Desnick, R.J., Willner, J.P., Friedman, T.B., and Griffith, A.J. (2003). Genetic homogeneity and phenotypic variability among Ashkenazi Jews with Usher syndrome type III. J. Med. Genet. *40*, 767–772.

41. Yang, D., Prieskorn, D., Song, J., Beyer, L., Dolan, D., Xu, J., Zhang, J., Raphael, Y., and YE, C. (2022). Rabbit Models of USH3A Have Progressive Hearing Loss. 45th Association for Research in Otolaryngology (ARO). Abst. *PD13*, p52–p53.

42. Kalra, G., Milon, B., Casella, A.M., Herb, B.R., Humphries, E., Song, Y., Rose, K.P., Hertzano, R., and Ament, S.A. (2020). Biological insights from multi-omic analysis of 31 genomic risk loci for adult hearing difficulty. Plos Genet. *16*, e1009025. https://doi.org/10.1371/journal.pgen.1009025.

43. Ivarsdottir, E.V., Holm, H., Benonisdottir, S., Olafsdottir, T., Sveinbjornsson, G., Thorleifsson, G., Eggertsson, H.P., Halldorsson, G.H., Hjorleifsson, K.E., Melsted, P., et al. (2021). The genetic architecture of age-related hearing impairment revealed by genome-wide association analysis. Commun. Biol. *4*, 706. https://doi.org/10.1038/s42003-021-02224-9.

44. Trpchevska, N., Freidin, M.B., Broer, L., Oosterloo, B.C., Yao, S., Zhou, Y., Vona, B., Bishop, C., Bizaki-Vallaskangas, A., Canlon, B., et al. (2022). Genome-wide association meta-analysis identifies 48 risk variants and highlights the role of the stria vascularis in hearing loss. Am. J. Hum. Genet. *109*, 1077–1091. https://doi.org/10.1016/j.ajhg.2022.04.010.

45. Boucher, S., Tai, F.W.J., Delmaghani, S., Lelli, A., Singh-Estivalet, A., Dupont, T., Niasme-Grare, M., Michel, V., Wolff, N., Bahloul, A., et al. (2020). Ultrarare heterozygous pathogenic variants of genes causing dominant forms of early-onset deafness underlie severe presbycusis. Proc. Natl. Acad. Sci. USA *117*, 31278–31289. https://doi.org/10.1073/pnas.2010782117.

46. Mianné, J., Chessum, L., Kumar, S., Aguilar, C., Codner, G., Hutchison, M., Parker, A., Mallon, A.M., Wells, S., Simon, M.M., et al. (2016). Correction of the auditory phenotype in C57BL/6N mice via CRISPR/Cas9-mediated homology directed repair. Genome Med. *8*, 16. https://doi.org/10.1186/s13073-016-0273-4.

47. Peineau, T., Belleudy, S., Pietropaolo, S., Bouleau, Y., and Dulon, D. (2021). Synaptic Release Potentiation at Aging Auditory Ribbon Synapses. Front. Aging Neurosci. *13*, 756449. https://doi.org/10.3389/fnagi.2021.756449.

48. Calvet, C., Peineau, T., Benamer, N., Cornille, M., Lelli, A., Plion, B., Lahlou, G., Fanchette, J., Nouaille, S., Boutet de Monvel, J., et al. (2022). The SNARE protein SNAP-25 is required for normal exocytosis at auditory hair cell ribbon synapses. iScience *25*, 105628. https://doi.org/10.1016/j.isci.2022.105628.

49. Quinodoz, M., Peter, V.G., Bedoni, N., Royer Bertrand, B., Cisarova, K., Salmaninejad, A., Sepahi, N., Rodrigues, R., Piran, M., Mojarrad, M., et al. (2021). AutoMap is a high performance homozygosity mapping tool using next-generation sequencing data. Nat. Commun. *12*, 518. https://doi.org/10.1038/s41467-020-20584-4.

**YMTHE, Volume *32***

## Supplemental Information

# Clarin-2 gene supplementation durably preserves hearing in a model of progressive hearing loss

**Clara Mendia, Thibault Peineau, Mina Zamani, Chloé Felgerolle, Nawal Yahiaoui, Nele Christophersen, Samantha Papal, Audrey Maudoux, Reza Maroofian, Pranav Patni, Sylvie Nouaille, Michael R. Bowl, Sedigheh Delmaghani, Hamid Galehdari, Barbara Vona, Didier Dulon, Sandrine Vitry, and Aziz El-Amraoui**

# SUPPLEMENTAL FIGURES

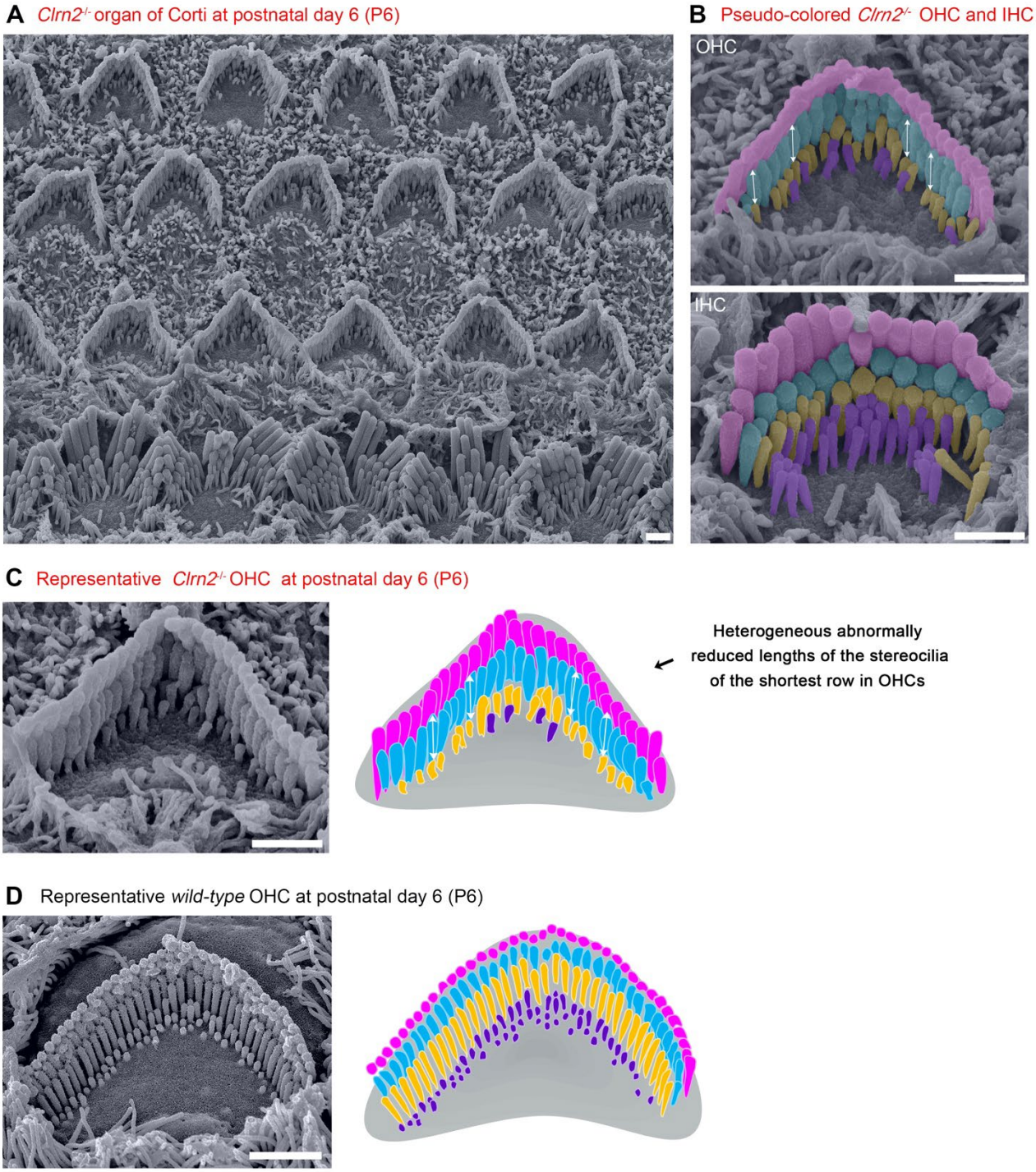


**Figure S1. Lack of clarin-2 leads to OHC hair bundle defects already by P6 immature postnatal stage.** **(A)** Representative scanning electron micrograph of the sensory epithelium of a P6 non-injected *Clrn2*$^{-/-}$ mouse. **(B)** Pseudo-colored images of individual hair cell bundles showing normal IHC bundle architecture but abnormal OHC bundle organization at P6. **(C-D)** Representative scanning micrographs, and their schematic diagrams, of P6 *Clrn2*$^{-/-}$ and wild-type OHCs. Scales, 1 µm.

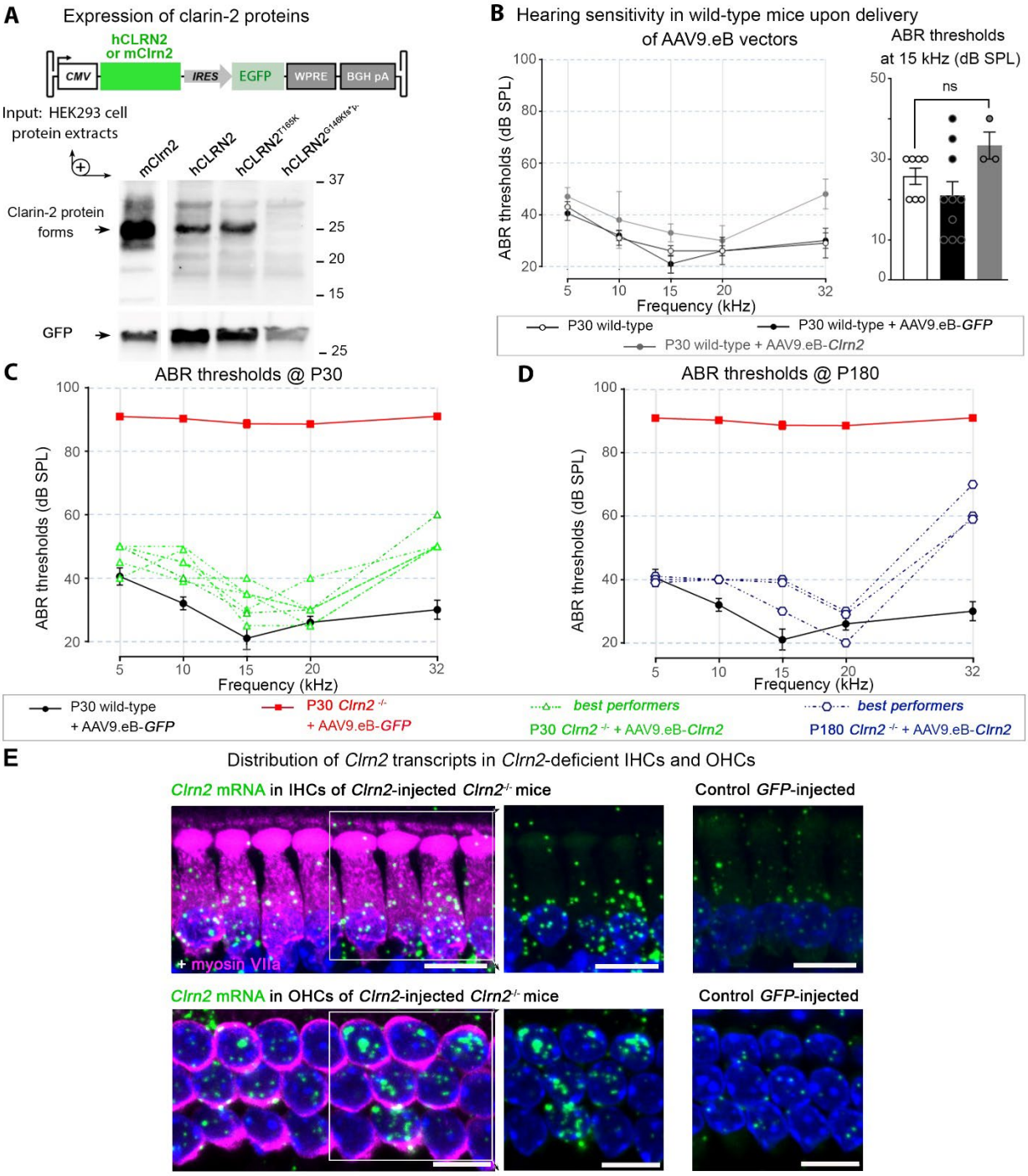


**Figure S2. Development and validation of a viral gene supplementation therapy targeting *Clrn2* deafness gene. (A)** Schematic diagram of the plasmids used to produce AAV9.eB vectors. Clarin-2 protein (25kDa) is immunodetectable by western blotting in HEK293 cells transfected with wild-type *mClrn2*, wild-type *hCLRN2* and mutated *hCLRN2*$^{T165}$. Note that our anti-Clarin-2 antibody (raised against Clrn2 C-terminal region) does not recognize the truncated form encoded by *hCLRN2*$^{G146KfsX26}$. As expected, GFP protein is detected in all cellular extracts. **(B)** Measurements of ABR thresholds in P30 wild-type mice injected or not with AAV9.eB-*GFP* or AAV9.eB-*Clrn2*, showing that both vectors are safe and do not alter hearing sensitivity. Data represent mean ± SEM from 3 to 10 mice per group. No significative difference between non-injected and AAV9.eB-*Clrn2* injected wild-type mice (p=0.7204, Kruskal-Wallis test). **(C)** ABR thresholds of the 7 best performers (green dotted lines) in the group of P30 *Clrn2*$^{-/-}$ mice injected at P1 with AAV9.eB-*Clrn2*. **(D)** ABR thresholds of the 3 best performers (dark blue dotted lines) in the group of P180 *Clrn2*$^{-/-}$ mice injected at P1 with AAV9.eB-*Clrn2*. **(E)** Confocal RNAscope images of organs of Corti of P8 *Clrn2*$^{-/-}$ mice injected at P1 with AAV9.eB-*GFP* or AAV9.eB-*Clrn2*, illustrating the mRNA expression pattern of *Clrn2* (green dots) in Myo7a-positive (magenta) IHCs and OHCs. Scales, 10 µm.

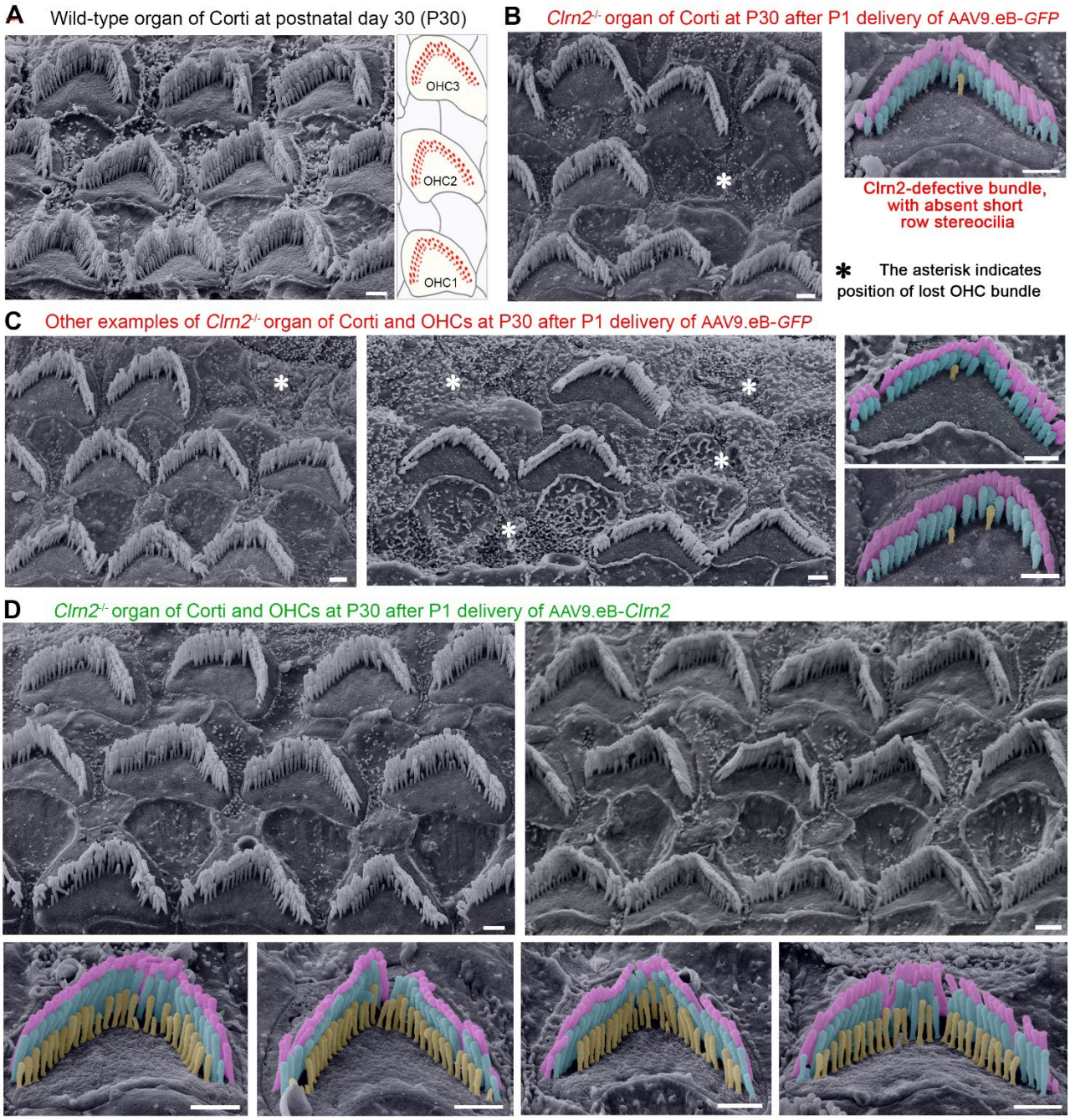


**Figure S3. *Clrn2* delivery successfully preserves the structure and stereocilia integrity of the auditory hair bundles. (A-D)** Representative scanning electron micrographs of the sensory epithelium of P30 wild-type mice (A) and P30 *Clrn2*$^{-/-}$ mice injected at P1 with AAV9.eB-*GFP* (B,C) or with AAV9.eB-*Clrn2* (D). Pseudo-colored images of individual OHC bundles show that AAV9.eB-*Clrn2* preserves the shortest row of stereocilia (yellow-colored). Scales, 1 µm.

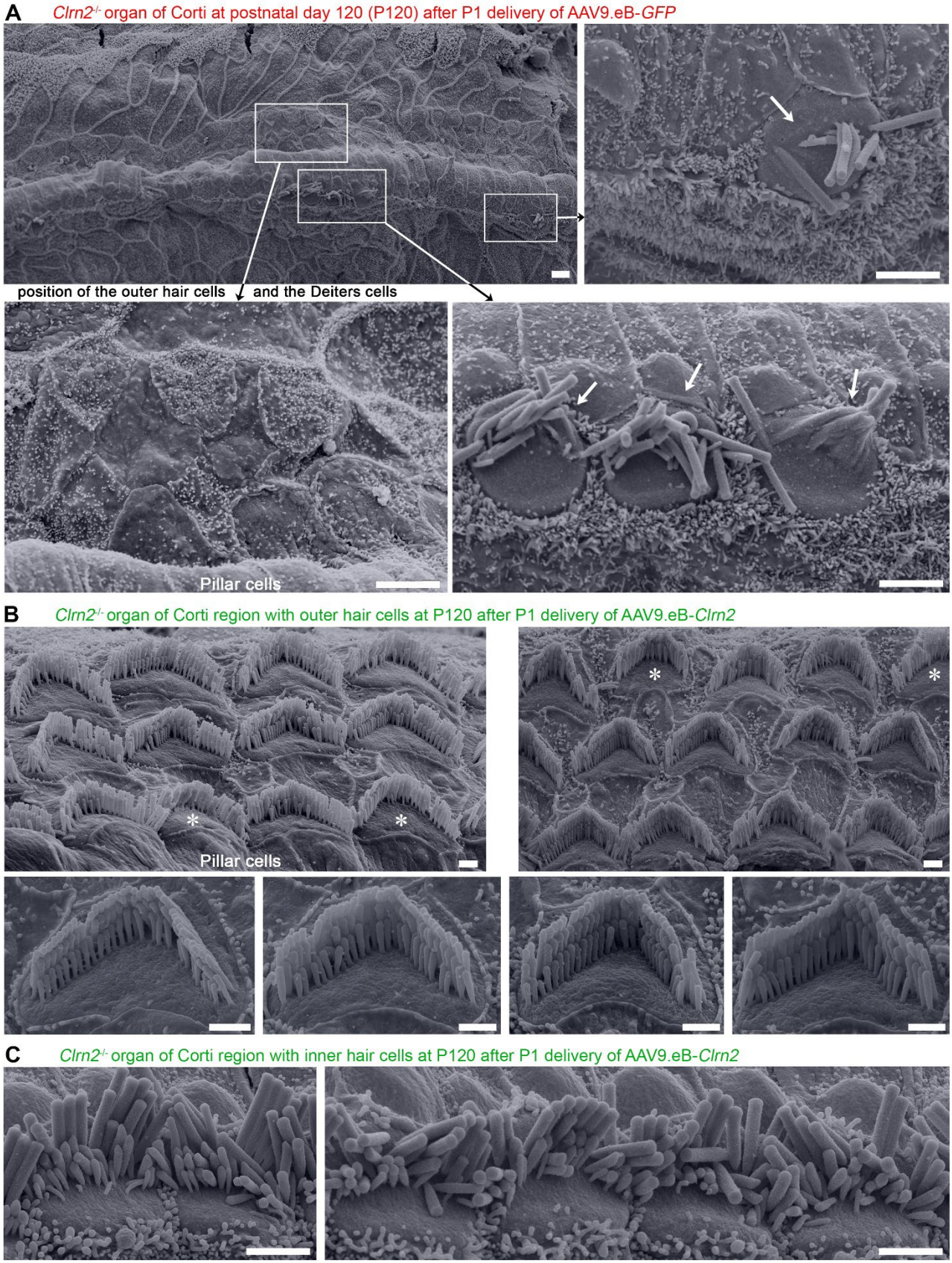


**Figure S4. Stable preservation of the hearing organ architecture in *Clrn2*$^{-/-}$ mice after neonatal *Clrn2* gene delivery. (A-C)** Representative scanning electron micrographs of the sensory epithelium of P120 *Clrn2*$^{-/-}$ mice injected at P1 with AAV9.eB-*GFP* (A) or with AAV9.eB-*Clrn2* (B,C) showing that AAV9.eB-*Clrn2* durably preserves OHC and IHC from death and their hair bundles from degeneration. Asterisks indicate OHCs with non-corrected short stereocilia rows. Scales, 1 µm.

**A** Homozygous regions for LI40734 Total = 232.32 Mb (autosomes)

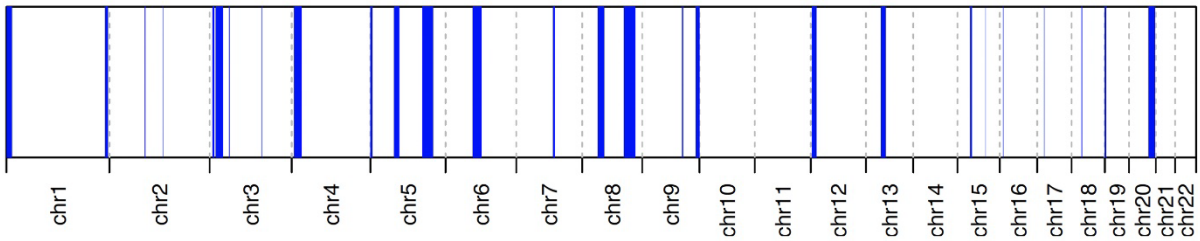


**B** Runs and coordinates of homozigosity

| | Begin | End | Size(bp) | Size (Mb) | Nb_variants | Percentage_homozygosity |
|---|---|---|---|---|---|---|
| chr1 | 187485 | 1634663 | 1447178 | 1.45 | 132 | 98.48 |
| chr1 | 1668449 | 13225044 | 11556595 | 11.56 | 357 | 98.04 |
| chr1 | 238907450 | 244970247 | 6062797 | 6.06 | 44 | 97.73 |
| chr2 | 85668215 | 87338620 | 1670405 | 1.67 | 52 | 94.23 |
| chr2 | 128980590 | 130356469 | 1375879 | 1.38 | 37 | 91.89 |
| chr3 | 7146429 | 11259021 | 4112592 | 4.11 | 86 | 98.84 |
| chr3 | 14526120 | 32159075 | 17632955 | 17.63 | 101 | 91.09 |
| chr3 | 46712480 | 48241004 | 1528524 | 1.53 | 57 | 92.98 |
| chr3 | 124977963 | 126159527 | 1181564 | 1.18 | 45 | 88.89 |
| **chr4** | **6085644** | **23884700** | **17799056** | **17.80** | **220** | **97.73** |
| chr5 | 163654 | 5232590 | 5068936 | 5.07 | 159 | 96.86 |
| chr5 | 57481850 | 69167187 | 11685337 | 11.69 | 68 | 89.71 |
| chr5 | 125360448 | 151563408 | 26202960 | 26.20 | 434 | 99.08 |
| chr6 | 65335034 | 86489515 | 21154481 | 21.15 | 100 | 96.00 |
| chr7 | 89336334 | 92448073 | 3111739 | 3.11 | 44 | 90.91 |
| chr8 | 38516406 | 52940311 | 14423905 | 14.42 | 104 | 100.00 |
| chr8 | 100721603 | 128087024 | 27365421 | 27.37 | 154 | 98.05 |
| chr9 | 96818812 | 98836929 | 2018117 | 2.02 | 53 | 94.34 |
| chr9 | 129620317 | 138217086 | 8596769 | 8.60 | 564 | 98.94 |
| chr12 | 3283185 | 9298611 | 6015426 | 6.02 | 246 | 97.56 |
| chr12 | 9298801 | 10434362 | 1135561 | 1.14 | 93 | 93.55 |
| chr12 | 11031153 | 13608807 | 2577654 | 2.58 | 58 | 93.10 |
| chr13 | 35828338 | 48001156 | 12172818 | 12.17 | 133 | 95.49 |
| chr15 | 30614056 | 32101283 | 1487227 | 1.49 | 29 | 93.10 |
| chr15 | 32451249 | 34527993 | 2076744 | 2.08 | 73 | 94.52 |
| chr15 | 67395630 | 68695002 | 1299372 | 1.30 | 27 | 92.59 |
| chr16 | 7653783 | 8746097 | 1092314 | 1.09 | 27 | 92.59 |
| chr17 | 16649599 | 17813391 | 1163792 | 1.16 | 36 | 88.89 |
| chr18 | 23540480 | 25224585 | 1684105 | 1.68 | 29 | 89.66 |
| chr19 | 287970 | 2732743 | 2444773 | 2.44 | 239 | 100.00 |
| chr20 | 47187946 | 62362541 | 15174595 | 15.17 | 204 | 95.59 |
| ## INFO: 232.32 Mb are in Homozygous Regions (autosomal chromosomes) | | | | | | |
| ## AutoMap v1.0 used for analysis | | | | | | |
| ## Variant filtering parameters used: DP=8, percaltlow=.25, percalthigh=.75, binomial=.000001, maxgap=10 | | | | | | |
| ## Other parameters used: window=7, windowthres=5, minsize=1, minvar=25, minperc=88, chrX=No, extend=1 | | | | | | |

**Figure S5. Homozygosity mapping in the *CLRN2* consanguineous family. (A)** Overview of the regions of homozygosity in the proband II:5 exome data totaling 232.32 Mb. **(B)** The *CLRN2*-containing homozygous region on chromosome 4 (yellow) is among the largest runs of homozygosity. Coordinates are shown in GRCh38 and sizes are summarized in base pair (bp) and megabases (Mb).

# SUPPLEMENTAL METHODS

### Quantitative real-time PCR

Freshly dissected inner ears were collected from P10 mice. Organs of Corti were micro-dissected in Dulbecco's phosphate buffered saline (DPBS), quickly frozen in liquid nitrogen and stored at -80°C until processing. Total RNAs were extracted in QIAZOL lysis reagent with miRNeasy Kit, according to the manufacturer's instructions. Total RNA (90 ng) was reverse transcribed with the SuperScript™ IV VILO™ Master Mix. RT-PCR products were digested with RNaseH. Purified cDNAs were then diluted in GoTaq® qPCR Master Mix containing BRYT Green Dye, in combination with QuantiTect primers targeting endogenous *Clrn2* gene (amplicon 944 bp), Clrn2 transgene (amplicon 699 bp) or RRN18S normalization gene. Quantitative real-time PCR reactions were performed in triplicate wells with a Quant Studio 6 Flex Real-Time PCR System (Applied Biosystems).

### RNA In situ hybridization (RNA ISH) of tissue

RNA-ISH was performed on wholemount organs of Corti using the RNAscope Multiplex Fluorescent Detection v2 kit. Mice were euthanized 7 days after AAV injection. Peri-auricular regions were taken out from the skull and fixed in 4% PFA for 1 hour at RT. Organs of Corti were micro-dissected and post-fixed in 4% PFA for 30 minutes at RT. After 3 washes in DPBS 0.1% Tween 20 (T-DPBS), samples were dehydrated in a graded methanol series (50%, 75%, 100%, 5 minutes each). After 10 minutes in 0.2M HCl diluted in 100% methanol, rehydratation in sequential methanol solutions (100%, 75%, 50%, 5 minutes each), 3 washes in T-DPBS, digestion with protease III for 20 minutes at RT and 3 washes in T-DPBS, tissues were hybridized with RNAscope Probe Mm-Clrn2-C3 for 8 hours at 40°C and post-fixed in 4% PFA for 10 minutes at RT. Hybridization Multiplex FL solutions were then sequentially applied at 40°C as follows : AMP1 for 35 minutes, AMP2 for 20 minutes, AMP3 for 35 minutes and HRP-C3 for 15 minutes. TSA Vivid Fluorophore kit 650 was then incubated 30 minutes at 40°C to reveal HRP. All these steps were alternated with double washes in Wash Buffer. HRP activity was then blocked with HRP blocker for 15 minutes at 40°C. Samples were then washed in T-DPBS and incubated for 1 overnight at 4°C with rabbit anti-Myosin VIIa antibody diluted in T-DPBS 0.2% BSA. After 2 washes in T-DPBS, an anti-rabbit IgG antibody conjugated to AlexaFluor 555 was used in combination with Hoechst nuclei dye for 1 hour at RT. Organs of Corti were lastly washed twice in T-DPBS and mounted in FluromountG. RNAscope positive and negative control probes were used to confirm the quality and specificity of the staining. Images were captured with a LSM700 confocal microscope piloted by the ZEN software (Zeiss). Z-stacks were imaged with a 40x oil immersion objective. Detectors were set to detect an optimal signal below saturation limits and staining panels were acquired during the same session using identical acquisition settings.

### Western blot

HEK293 cells were maintained in DMEM/F-12 GlutaMAX supplemented with 10% fetal bovine serum and Penicillin/Streptomycin, and incubated at 37°C 5 % CO2. Cells (70-90% confluency) were transfected with

the plasmids used to produce AAV vectors, in the presence of Lipofectamine 3000 following the manufacturer's protocol. After 48 hours of incubation, total protein extracts of transfected cells were prepared by using RIPA lysis buffer, supplemented with an EDTA-free cocktail of protease inhibitors (Complete Ultra). Lysates were cleared by centrifugating 17,000g for 20 minutes at 4°C. Supernatants were collected and protein content measured using Bicinchoninic Acid (BCA) protein assay. Equal protein amounts were diluted in Laemmli buffer, heated at 95°C for 5 minutes then submitted to SDS/PAGE on 12% polyacrylamide gel and transferred to a PVDF membrane. Blotted membranes were incubated with anti-GFP or anti-Clarin-2 antibodies followed by Horseradish peroxidase (HRP)-conjugated secondary antibodies and revealed with Clarity Western ECL Substrate.

**Table S1 : List of Reagents. Supplied separately as an Excel file.**